

Robust Chemiresistive Behavior in Conductive Polymer/MOF Composites

Heejung Roh, Dong-Ha Kim, Yeongsu Cho, Young-Moo Jo, Jesús A. del Alamo, Heather J. Kulik, Mircea Dincă,* Aristide Gumyusenge**

H. R., Dr. A. G.

Massachusetts Institute of Technology, Department of Materials Science & Engineering,
77 Massachusetts Ave, Cambridge, MA, 02139, USA

Email: aristide@mit.edu

H. R., Dr. D.-H. K., Dr. Y.-M. J., Dr. M. D.

Massachusetts Institute of Technology, Department of Chemistry, 77 Massachusetts Ave,
Cambridge, MA, 02139, USA

Email: mdinca@mit.edu

Dr. Y. C., Dr. H. J. K.

Massachusetts Institute of Technology, Department of Chemical Engineering, 77 Massachusetts
Ave, Cambridge, MA, 02139, USA

Massachusetts Institute of Technology, Department of Chemistry, 77 Massachusetts Ave,
Cambridge, MA, 02139, USA

Email: hjkulik@mit.edu

Dr. J. A. A.

Massachusetts Institute of Technology, Department of Electrical Engineering and Computer
Science, 77 Massachusetts Ave., Cambridge, MA, 02139, USA

MIT-IBM Watson AI Lab, 75 Binney St., Cambridge, MA, 02139, USA

Keywords: conjugated polymers, metal-organic frameworks, composites, chemiresistors

Abstract

Metal-organic frameworks (MOFs) are promising materials for gas sensing but are often limited to single-use detection. We demonstrate a hybridization strategy synergistically deploying

conductive MOFs (*c*MOFs) and conductive polymers (*c*Ps) as two complementary mixed ionic-electronic conductors in high-performing stand-alone chemiresistors. Our work presents significant improvement in i) sensor recovery kinetics, ii) cycling stability, and iii) dynamic range at room temperature. We demonstrate the effect of hybridization across well-studied *c*MOFs based on 2,3,6,7,10,11-hexahydroxytriphenylene (HHTP) and 2,3,6,7,10,11-hexaiminotriphenylene (HITP) ligands with varied metal nodes (Co, Cu, Ni). We conduct a comprehensive mechanistic study to relate energy band alignments at the heterojunctions between the MOFs and the polymer with sensing thermodynamics and binding kinetics. Our findings reveal that hole enrichment of the *c*MOF component upon hybridization leads to selective enhancement in desorption kinetics, enabling significantly improved sensor recovery at room temperature, and thus long-term response retention. This mechanism was further supported by density functional theory calculations on sorbate-analyte interactions. We also find that alloying *c*Ps and *c*MOFs enables facile thin film co-processing and device integration, potentially unlocking the use of these hybrid conductors in diverse electronic applications.

1. Introduction

Metal organic frameworks (MOFs) are attractive for catalysis, energy storage, chemical capture, as well as sensing owing to their inherent porosity, high surface area, and high molecular absorptivity.^[1-5] Particularly for MOF-based sensing, the chemical versatility of metal nodes and organic ligands renders MOFs attractive for molecularly tuning both sensitivity and selectivity towards a wide range of analytes.^[6,7] Pore size control also provides an additional knob for size-exclusion based sensing.^[8-10] Electrically conductive MOFs (*c*MOFs) are of particular interest in chemiresistive sensors leveraging their conductance modulation within the framework upon host-guest interaction to identify and quantify the guest molecules.^[11,12] However, deploying *c*MOFs in sensors still faces technological challenges: i) MOFs are commonly synthesized as powders and their integration into electronic devices is challenging. Typically, MOF powders are pressed into pellets or suspended as pastes to form active layers, leading to poor performance reproducibility and loss in inherent properties at the expense of additive loadings.^[13-15] Layer-by-layer liquid epitaxy and surface-supported MOF growth, though yet to be demonstrated for a wide library of MOF structures, have emerged as promising alternative processing strategies for applications

requiring high quality thin films.^[16–18] ii) MOF-based chemical sensors are often dosimetric due to limited reversibility which hinders practical use.^[19,20]

Particular to gas sensing, *c*MOF-based detection of gases typically involves a combination of physical adsorption and chemical interactions.^[5] For instance, ligand designs to form electron rich coordination sites favorable for attracting ubiquitous polar gas molecules through Van der Waals interactions have been demonstrated.^[5] In addition, transition-metal nodes in these *c*MOFs primarily drive the majority of chemiresistive sensing owing to strong Lewis acid-base reactions between the metal nodes and analytes, especially polar gas molecules.^[19,21,22] Consequently, 2D-conjugated ligands, namely 2,3,6,7,10,11-hexahydroxytriphenylene (HHTP) and 2,3,6,7,10,11-hexaminotriphenylene (HITP), in combination with common nodes (Cu, Ni, Co) have been widely studied in chemiresistive gas sensors owing to their excellent and tunable electrical conductivity (which enables detection based on resistance change), as well as their facile synthesizability.^[18,23–25] In that regard, gases such as NH₃, H₂S, and other volatile organic compounds have been reliably detected using *c*MOF-based sensors.^[24]

NO₂ is one of the commonly emitted toxic gases that remains challenging to detect, even using conductive MOFs, especially at room temperature. Though *c*MOFs have shown promising performance for NO₂ detection,^[26] irreversible sensing remains a major challenge due to the formation of stable coordination complexes, a trait that enables high sensitivity. Reversible detection of NO₂ at room temperature using MOFs becomes an inherent challenge due to strong binding behaviors, arising from NO₂'s tendency to extract electrons from metal nodes (e.g., Cu¹⁺) and form coordination complexes (e.g., (1) N-nitro, (2) O-nitrito, or (3) O, O' bidentate)^[27,28] following the reaction below:



Due to this charge transfer, the *c*MOF's electron density distribution is perturbed thus translating into detectable resistance changes. *c*MOF-based chemiresistors have thus been studied as a promising technology for NO₂ gas sensing.^[24] To achieve sensor reversibility, approaches such as the use of elevated temperature, incorporation of noble metal catalysts, and photoactivation utilizing specific wavelength, and incorporation of heavy-metal nanoparticles have been reported to improve recovery kinetics, which still hamper real-world deployments.^[21,22,24,29] In fact, these

approaches remain the state-of-the-art, despite unique and promising features of *c*MOFs for NO₂ detection.^[24,30] For real-world use, these approaches remain too costly, challenging to generalize, and user unfriendly, thus calling for innovative strategies to fully leverage the affinity of MOFs towards NO₂.

Efforts to expand the library of MOFs used in sensing applications have led to the utilization of polymer/MOFs hybrids when direct film growth of MOFs is challenging.^[13–15] However, this approach often results in a compromise between processability and inherent properties. That is, MOFs are typically blended with polymer additives, which are often insulating polymers, thus masking the intrinsic properties of the MOF components.^[13–15] Here we report a new concept to synergistically marry sensing performance and processability especially for detecting NO₂ gas at room temperature. We form hybrid films using designer conjugated polymers (*c*Ps) and conductive MOFs to improve: (i) The sensitivity compared to pristine *c*MOFs, stemming from increased density of the active material in the sensor. (ii) Chemical selectivity via the incorporation of systematically functionalized *c*Ps with selective and labile binding with NO₂. (iii) Regeneration of active sites within the sensing material, and consequently, long-term reliability at room temperature, due to improved kinetics of molecular exchange and a thermodynamically enhanced desorption process. And lastly, (iv) solution processibility via facile deployment methods (e.g., spin-coating, blade-coating, screen-printing, etc.), which is not readily unattainable in pristine MOFs.

2. Results and Discussion

2.1. Designing conductive polymer/MOF films for chemiresistive devices

To form the newly designed polymer/MOF composite, we use a semicrystalline, mixed ionic-electronic conductive polymer (*c*P) based on 3,4-propylenedioxythiophene (ProDOT) and 2,1,3-benzothiadiazole (BTD),^[31] and form hybrid films with 2D *c*MOFs (**Fig. 1 a-c** and **Supplementary Fig. 1, 2**). We select the ProDOT-BTD *c*P for its reversible redox-activity, low onset oxidation voltage, charge capacity, electrical conductivity to enhance the device response in presence of the analyte.^[32,33] Particularly, the *c*P is designed to serve as a secondary NO₂-affine component endowed by its polar sidechains,^[34–37] as well as a binding matrix to physically unify *c*MOFs crystallites and improve electrical communication throughout the bulk (**Fig. 1 c,d**). We

then select two classes of *c*MOFs based on 2,3,6,7,10,11-hexahydroxytriphenylene (HHTP) and 2,3,6,7,10,11-hexaiminotriphenylene (HITP) ligands (**Fig. 1 a**), which typically exhibit irreversible gas sensing behaviors in their pristine form. As shown in **Fig. 1 e** and **Supplementary Fig. 2**, the x-ray diffraction peaks corresponding to pristine *c*MOFs remain unchanged upon hybridization without peak shifts, indicating that the structure of the *c*MOF remains undisturbed and well-preserved. We then study diverse metal nodes, which have shown promising performance in chemiresistive devices via molecular interactions between analyte gases and coordination sites.^[38] All six *c*MOF combinations, namely $M_3(\text{ligand})_2$, where M is either Co, Ni, or Cu and the ligand HHTP (X=O) or HITP (X=NH), were first synthesized and respective structures were verified through powder x-ray diffraction (PXRD) analysis (**Supplementary Fig. 2**).

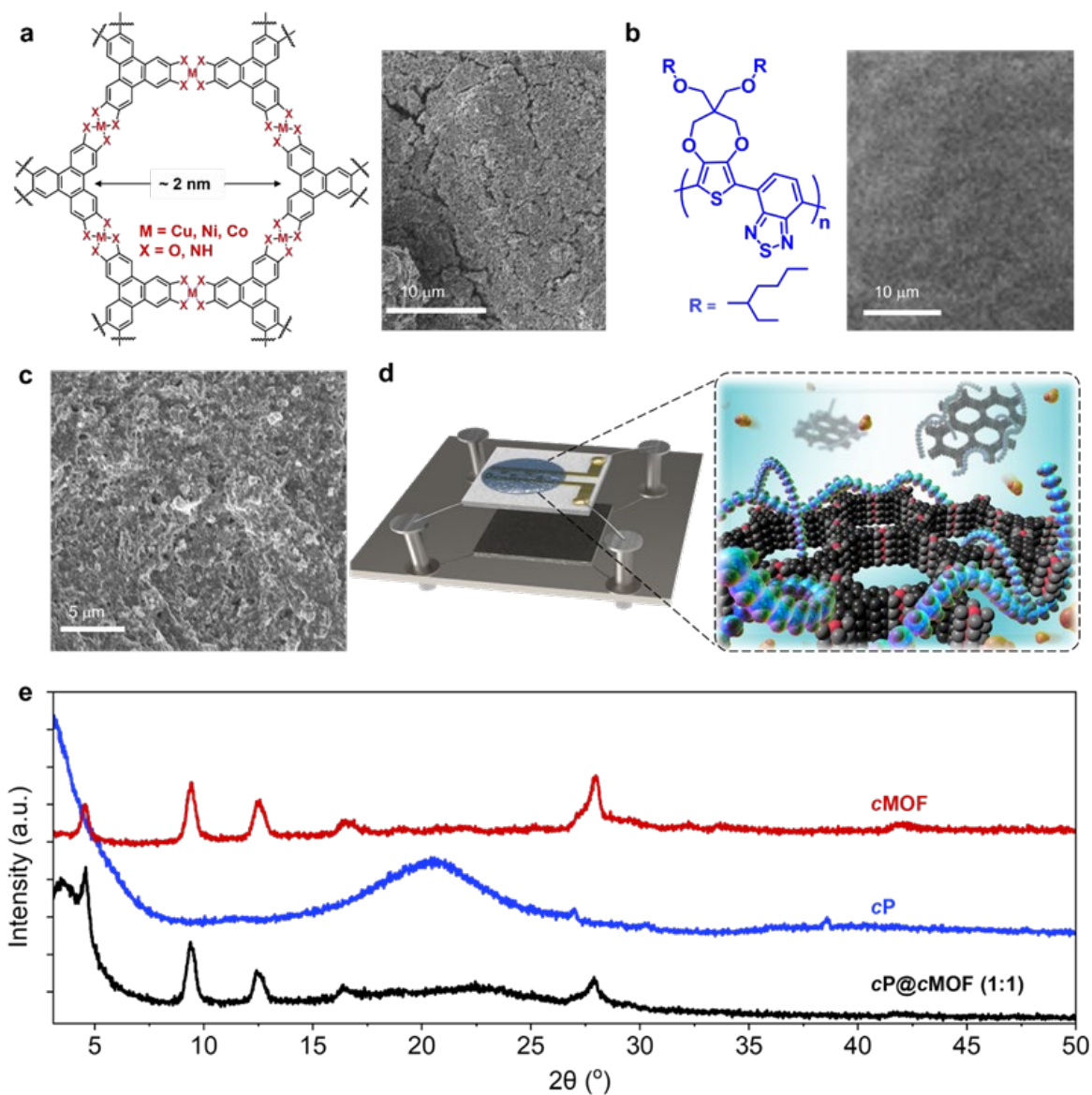


Figure 1. Hybridization between conductive polymers and MOFs for robust chemiresistors. (a), (b) Chemical structure and representative SEM images of 2D *c*MOFs, $M_3(\text{ligand})_2$ (e.g., Cu_3HHTP_2) and *c*P. (c) SEM image of *cP@c*MOFs (1:1, w/w). (d) Schematic illustration of sensing device and interaction between *cP@c*MOF and gas analyte. (e) PXRD spectra of 2D *c*MOF (Cu_3HHTP_2), *c*P, and corresponding *cP@c*MOFs (1:1, w/w).

Scanning electron microscope (SEM) images show that the hybrid *cP@c*MOFs films are homogeneous and *c*MOFs crystallites are uniformly embedded in the *c*P matrix (e.g., *cP@c* Cu_3HHTP_2 , **Fig. 1 c**). This is in contrast with pristine *c*MOF films which show micro-cracks and pristine *c*P with a smooth texture (**Fig. 1 a,b**). We also use atomic force microscopy (AFM) imaging to compare surface roughness of drop-casted films, revealing smoother surfaces in

cP@cMOFs compared to pristine *cMOFs* with R_q values of 97.5 nm and 195 nm, respectively, owing to the presence of the *cP* with R_q value of 22.7 nm (**Supplementary Fig. 3a-c**). Furthermore, as corroborated by surface analysis using x-ray photoelectron spectroscopy (XPS) and Raman spectroscopy (probing depths of 10 nm and 645 nm, respectively), the *cP* shows to constitute most of the outermost layer of the composite films (at least ~ 10 nm), engulfing *cMOFs* crystallites. At such shallow depths, the distinctive metal peaks from the *cMOF* component were absent in high-resolution XPS spectra of hybrid films (**Supplementary Fig. 4**). At the same time, corresponding Raman spectra were identical to that of pristine *cP* (**Supplementary Fig. 5**) indicative of a predominantly polymer-enriched interface in the hybrid films. We hypothesize that with this architecture, the semicrystalline and NO_2 -affine polymer would also contribute to the adsorption of gas molecules into sensor's channel area and enhance the overall sensitivity of the sensors. That is, i) the conductive backbone is flanked with polar sidechains favoring the permeability of gas molecules into the active area across entire active channel,²⁹⁻³² and ii) *cP* serves as a conductive matrix binding together the MOF crystallites throughout the bulk, thus promoting efficient charge transport upon resistance change. By interlinking the crystallites throughout the film bulk, the *cP* thus helps reduce inter-particles resistance, a dominant behavior in pristine MOFs, and enhances the performance of chemiresistors based on polymer/MOF composites (**Fig. 1 c,d**). The pasty nature of the solution processed *cP* was also envisioned to promote greater films integrity and hence device reliability and stability.

2.2. Gas sensing performance of *cP@cMOFs*

To test the effect of hybridization on gas sensing performance, we fabricated chemiresistive sensors using the *cP@cMOFs* combinations discussed above. Further details on the sensor fabrication steps and device dimensions are provided in the experimental section and illustrated in **Supplementary Fig. 6**. As shown in **Fig. 2 a**, all sensors based on pristine *cMOFs* exhibited relatively low responses ($R_{\text{air}}/R_{\text{gas}}$ or $R_{\text{gas}}/R_{\text{air}} < \sim 2$, where R_{air} and R_{gas} denote resistance in air and gas, respectively) as well as poor sensing reversibility. Upon hybridization with *cP* (e.g., 1:1 weight ratio between *cP* and *cMOF*), the sensing response, and most importantly, the sensing reversibility was significantly enhanced across all *cMOFs* (**Fig. 2 a-c** and **Supplementary Fig. 7**). This performance enhancement was most exemplified in *cP@Ni₃(HITP)₂* exhibiting a 23.9-fold improvement in sensor response relative to pristine *Ni₃(HITP)₂* (**Fig. 2 c**). Note that, in its pristine

form the *cP* yields sensors with undetectable response, and the same effect could not be induced when the hybridization is done with corresponding ligands (HHTP or HITP) instead of *cMOFs*, or other commonly studied conductive materials such as carbon nanotubes (CNTs) (**Supplementary Figs. 8, 9**). This behavior thus underscores the importance of utilizing a conductive polymer to hybridize with the porous *cMOFs* and synergistically enhance sensing response and reversibility.

Furthermore, the hybridization was beneficial to the sensitivity level of the sensor devices as illustrated in the dynamic resistance changes with NO₂ concentrations down to 0.25 ppm (**Fig. 2 d-f**). In terms of sensitivity, we found that, upon optimization of the *cP* content in the hybrid films (**Supplementary Figs. 10-15**), *cP@Ni₃(HITP)₂* demonstrated the most pronounced initial response in the presence of NO₂, albeit its relatively modest reversibility compared to the *cP@Co₃(HHTP)₂* analogue. Also noteworthy, among all hybrid combinations, *cP@Co₃(HHTP)₂* exhibited the most dynamic resistive behavior and reversibility enhancement in comparison to its pristine counterpart. Nonetheless, across all six *cMOFs*, the hybridization showed to enhance the sensing response compared to pristine constituents (**Fig. 2 g**) while conserving the selectivity level towards NO₂ gas (**Supplementary Figs. 16, 17**), given uniform distribution of the components within the bulk (**Supplementary Fig. 18**). Most importantly, all *cP@cMOFs*-based sensors demonstrated enhanced cycling reversibility compared to their pristine counterparts (**Fig. 2 h-i** and **Supplementary Figs. 10,14**). Particularly, *cP@Co₃(HHTP)₂*-based sensors exhibit stable and reversible performance up to 97 cycles (**Fig. 2 h-i**). To the best of our knowledge, our work presents the highest number of cycling tests with stable reversibility among all *cMOFs*- or *cP*-based chemiresistive sensors reported to date (**Table 1**).^[21]

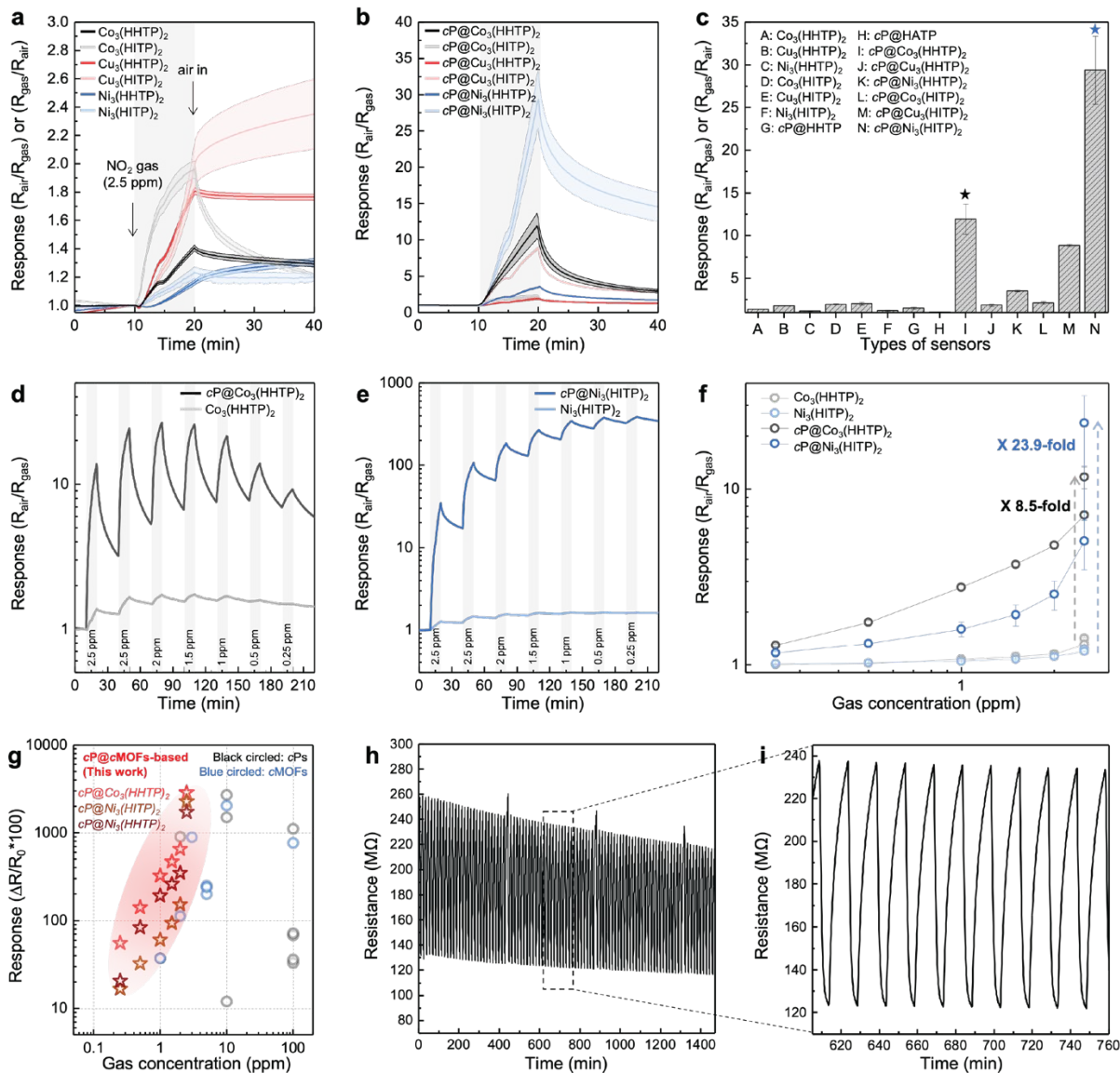


Figure 2. Sensing performance evaluation in $cP@cMOF$ -based chemiresistors. Response graphs of (a) 6 different pristine $cMOFs$ and (b) $cP@cMOFs$ with 1:1 ratio. (c) Response of all the sensors including pristine $cMOFs$, $cP@ligands$, and $cP@cMOFs$ ($N \geq 3$). (d) Response graphs of $Co_3(HHTP)_2$ and $cP@Co_3(HHTP)_2$ toward 2.5-0.25 ppm NO_2 gas. (e) Response graphs of $Ni_3(HITP)_2$ and $cP@Ni_3(HITP)_2$ toward 2.5-0.25 ppm NO_2 gas. (f) Response of $Co_3(HHTP)_2$, $Ni_3(HITP)_2$, $cP@Co_3(HHTP)_2$, and $cP@Ni_3(HITP)_2$ toward 2.5-0.25 ppm NO_2 gas ($N \geq 3$). (g) Responses of reported NO_2 sensors using cP or $cMOFs$, operating at RT.^[19,21,22,29,39-50] (h) Operational stability of a $cP@Co_3(HHTP)_2$ sensor under 97 cyclic exposures (1 ppm NO_2 , 5 min exposure, 10 min air recovery), including (i) an enlargement around $t = 605-760$ min.

Sensing material	Response [$\Delta R/R_0 * 100 \%$]	Cyclability (# of cycles)	LOD [ppm]	Ref.
PPy thin film	12 @ 10 ppm	3	10	39
PT thin film	33 @ 100 ppm	3	10	40
PANI-nanofibers	1500 @ 10 ppm	n.r.	10	41
PANI thin film	1110 @ 100 ppm	n.r.	10	42
Ag-PPy	68 @ 100 ppm	n.r.	5	43
PANI fibers	900 @ 2 ppm	n.r.	1	44
ZnO/PANI nanoflake	2700 @ 10 ppm	n.r.	0.01	45
DBSA-doped PPy-WO ₃	72 @ 100 ppm	3	5	46
PPy/ α -Fe ₂ O ₃	36 @ 100 ppm	3	10	47
PEI-doped PNDIT2/IM	37.2 @ 1 ppm	15	0.1	48
Cu ₃ (HHTP) ₂ /Fe ₂ O ₃ hybrids	~200 @ 5 ppm	7	0.2	21
Pd@Cu ₃ (HHTP) ₂	~250 @ 5 ppm	14	1	22
Pt@Cu ₃ (HHTP) ₂	~240 @ 5 ppm	14	1	19
PtRu@Cu ₃ (HHTP) ₂	112.8 @ 2 ppm	7	0.2	19
Pt@Cu ₃ (HHTP) ₂ thin film	890.1 @ 3 ppm	n.r.	0.1	26
Cu-Salphen-MOF	766 @ 100 ppm	5	1	50
Single crystal Ti-MOF (FIR-120)	2040 @ 10 ppm	5	1	29
cP@CoHHTP 1:4	2863 @ 2.5 ppm	97	0.25	This work
cP@NiHHTP 1:1	2282 @ 2.5 ppm	10	0.25	This work
cP@NiHHTP 8:1	1716 @ 2.5 ppm	10	0.25	This work

Table 1. Comparison of current results to state-of-the-art NO₂ sensing at room temperature using cPs- and cMOFs-based chemiresistors (n.r.: not reported).

2.3. The role of hole enrichment toward reversible NO₂ sensing

Key to synergistically deploying both conductors in our hybrid films is the electronic characteristic at the heterojunctions formed between cP and cMOFs, as well as the distribution of such heterojunctions throughout the bulk. Particularly, the activation energy for charge carrier transport in response to NO₂ adsorption is pivotal for enhancing the sensing performance of hybrid films. Here we sought to evaluate the sensor reversibility at room temperature by monitoring the channel resistance recovery before and after NO₂ exposure. As discussed above and confirmed by solid state characterizations, the structural configuration of the hybrid film (i.e., lowered film crystallinity and uniform distribution of cMOF crystallites within the cP bulk) accounts for

enhancement in sensitivity and its retention. Given that our *cP@cMOFs*-based sensors also exhibit excellent signal recovery, we sought to mechanistically understand the impact of these features on the adsorption and desorption kinetics of NO₂ gas. In MOF-based NO₂ sensors, reducing the sensor response times and, more importantly, increasing the desorption rate constant (k_{des}) to achieve reversible sensing has been challenging.^[26]

Without relying on external stimuli or addition of inactive components, the newly designed *cP@cMOFs* hybridization provides a thermodynamic solution to irreversible detection of NO₂. The experimentally constructed energy band diagrams showing respective HOMO levels with respect to fermi level reveal p-type *cP* as the most hole-rich component (**Fig. 3 a** and **Supplementary Figs. 19, 20** and **Table S1**). In all studied *cMOF* cases, the two materials are energetically close enough allowing us to hypothesize that, upon hybridization, beyond the formation of microscopic interfaces throughout the bulk, the *cP-cMOF* heterojunctions establish an electronic equilibrium, and the majority carriers occupy a shared Fermi level (**Fig. 3 a**). In other words, a hole transfer from the *cP* to the *cMOF* is thermodynamically favorable forming a hybrid and hole-enriched *cMOF* state (**Fig. 3 a** and **Supplementary Figs. 20, 21**).^[51,52] This injection of holes into the *cMOF*'s electronic configuration alters the interaction between NO₂ and the sensing channel by lowering the binding energy (the primary source of irreversible sensing, **Supplementary Fig. 22**), resulting in reversible sensing behavior, even at room temperature (**Fig. 3 a**). Prior to this work, the desorption of NO₂ gas from MOF sorbate materials has been achieved using elevated temperatures, high energy radiation, or the incorporation of heavy metals in the active layer.^[26] The hybridization strategy we report here is much more straightforward and holds potential for generalization onto essentially any conductive MOF structure.

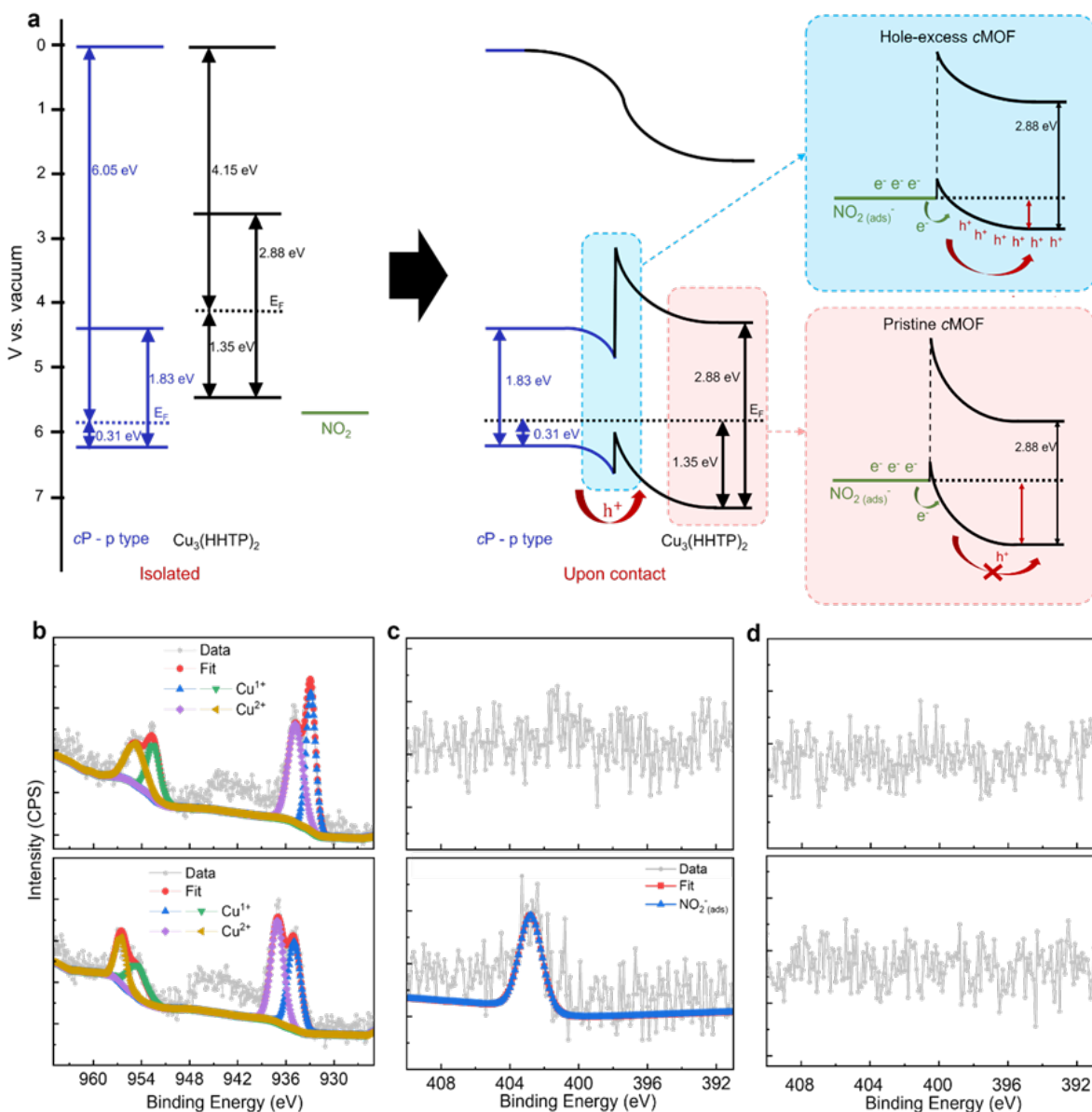


Figure 3. Hole enrichment in cMOFs and its impact on analyte binding. (a) Experimentally constructed energy level diagram of cP and representative cMOF (full data for all cMOFs studied can be found in **Supplementary Figs. 19,20**) and proposed mechanism/rationale for enhanced recovery upon hybrid. (b) High resolution XPS spectra of Cu 2p peak region, before (top) and after (bottom) NO₂ exposure. (c, d) High resolution XPS spectra of N 1s peak region of (c) Cu₃(HHTP)₂ and (d) cP@Cu₃(HHTP)₂, respectively, before (top) and after (bottom) NO₂ exposure.

To test our proposed working mechanism, we first examined the XPS spectra of the active material before and after NO₂ exposure. The oxidative effect of NO₂ on the sensing materials was evidenced by subsequent charge redistribution around the metal nodes to compensate the charge imbalance. High-resolution XPS spectra of the characteristic metal peaks (e.g., Cu 2p) reveal a

significant change in the ratio between oxidation states of the metal (e.g., Cu¹⁺ and Cu²⁺). In the case of Cu₃(HHTP)₂ films, substantial change in the oxidation state of the Cu was evidenced by a decrease in the Cu¹⁺ (~933 eV)/Cu²⁺ (~935 eV) ratio from 1.17 to 1.09 after exposure to NO₂ (**Fig. 3 b**). Concomitantly, in the pristine MOF samples, despite the high vacuum conditions during XPS measurements, the adsorption and binding of NO₂ molecules was evidenced by a signature peak at 403.9 eV (**Fig. 3 c**). In contrast, the hybrid films exhibit no discernable signal from this N 1s peak within the same desorption timescale (**Fig. 3 d**), indicative of nearly complete desorption of NO₂ gas from the hybrid films. We associate this complete desorption to the formation of a new Fermi level upon hole enrichment, thus weakened binding between the gas molecules and the *c*MOF sites. This labile binding between NO₂ molecules and our *cP@c*MOFs films would thus be the key rationale to the observed dynamic response in the chemiresistive sensors.

We further corroborated this sensing mechanism by experimentally monitoring the sensor's recovery kinetics upon hybridization. We employed a mass action law of gas adsorption reactions on both *c*MOFs and *cP@c*MOFs and computed the response and recovery kinetics for NO₂ sensing. Our calculations assumed that the quantity of gas adsorbed on the surface is directly related to the sensors' response. We then calculated respective rate constants according to previous works (i.e., *k*_{ads} for gas adsorption and *k*_{des} for the desorption)^[53,54] by fitting the sensor's response graphs using equations (1) and (2) below for six distinct *c*MOFs and corresponding *cP@c*MOFs (**Supplementary Fig. 23**):

$$R(t) \text{ for NO}_2 \text{ adsorption} = R_{\max} \cdot \frac{C_a K}{1 + C_a K} \left(1 - \exp \left[-\frac{1 + C_a K}{K} \cdot k_{\text{ads}} t \right] \right), \quad (1)$$

$$R(t) \text{ for NO}_2 \text{ desorption} = R_0 \exp[-k_{\text{des}} t]. \quad (2)$$

Here, *R*₀ is the baseline response in air, *R*_{max} is the maximum response, *C*_a is the gas concentration, *t* is time, and *K* is an equilibrium constant (*k*_{ads}/*k*_{des}).^[53] In all cases, *cP@c*MOFs displayed remarkably improved desorption kinetics compared to their corresponding pristine *c*MOFs counterparts. Notably, the *k*_{des} for *cP@c*Cu₃(HITP)₂ was measured to be 93.7-fold higher compared to that of pristine Cu₃(HITP)₂. Interestingly, the *k*_{ads} values for all *cP@c*MOFs exhibited minimal changes when compared to those of pristine *c*MOFs. It was thus evident that the dominant factor for enhancing reversibility in the composite systems is the thermodynamic effect from the hole enrichment, rather than structural factors. Note that for Cu₃(HITP)₂ and Ni₃(HHTP)₂, which

showed n-type resistive variation upon NO₂ exposure (oxidizing gas), a higher amount of cP was required than other cMOFs to achieve the optimal ratio for reversibility (**Supplementary Figs. 10-12, 14**). Serendipitously, these two systems also exhibit significantly larger ($E_F - E_V$) values relative to the cP in energy level diagram, making the hole enrichment more energy consuming. With the same rationale, superior room temperature reversibility was observed in pristine Co-based cMOFs compared to other pristine cMOFs and could be attributed to their notably lower ($E_F - E_V$) value (~ 0.5 eV) (thus inherent abundance of hole carrier density), set aside lower crystallinity (**Supplementary Fig. 24**).

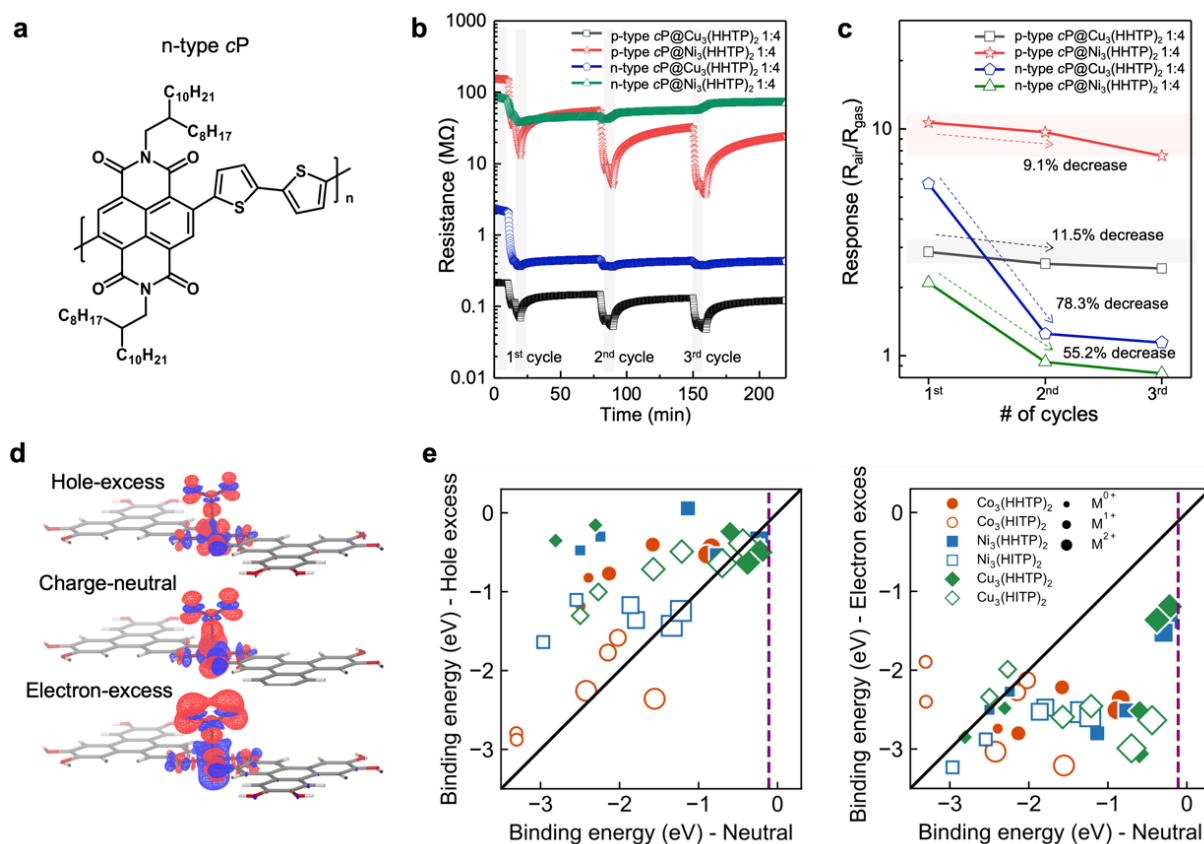


Figure 4. Relationship between binding energy and sensor performance. (a) Chemical structure of n-type polymer studied. (b) Dynamic resistance transitions with varied types of polymers in hybrid. (c) Response profile with varied types of polymers in hybrid. (d) Differences in charge density before and after NO₂ binding to the cMOF cluster for three system conditions: hole-excess, charge-neutral, and electron-excess, calculated as $\rho(\text{Cluster} + \text{NO}_2) - \rho(\text{Cluster}) - \rho(\text{NO}_2)$, where ρ is the charge density. The red surface denotes an increase in charge density upon NO₂ binding, while the blue surface denotes a decrease. An iso-surface value of $0.0025 \text{ e}^{-1}/\text{\AA}^3$ has been applied. (e) Binding energy of cMOF and NO₂ when the cMOF has an excess hole (left)

and an excess electron (right), compared to charge-neutral *c*MOF. Both adsorption cases, where NO₂ binds either through the O or N atom, are illustrated. The purple dashed line represents the average binding energy between the *c*P and NO₂. The black solid line indicates parity.

To verify the role of hole enrichment and test potential countereffect from electron enrichment, we substituted the *c*P component in our hybrid films with an n-type polymer (in this case, poly {[N,N'-bis(2-octyldodecyl)-naphthalene-1,4,5,8-bis(dicarboximide)-2,6-diyl]-alt-5,5'-(2,2'-bithiophene)}, also known as N2200) (**Fig. 4 a**). We then fabricated four types of sensors, i.e., p-type *c*P@Cu₃(HHTP)₂, p-type *c*P@Ni₃(HHTP)₂, n-type *c*P@Cu₃(HHTP)₂, and n-type *c*P@Ni₃(HHTP)₂, and compared their sensing behavior under similar conditions. More specifically, we monitored the channel resistance recovery after 3 cyclic exposures of the sensor to 2.5 ppm NO₂. P-type *c*P-based composites exhibited reversible sensing behaviors with minimal reduction in response, 9.1% and 11.5%, respectively, after the first cycle NO₂ exposure (**Fig. 4 b,c**). Conversely, n-type *c*P-based composites demonstrated a dramatically diminished response after the first cycle. Furthermore, exposure to higher NO₂ concentrations in subsequent cycles showed no further change in the channel resistance for n-type composites (**Supplementary Fig. 25**) indicative of a dosimetric sensing behavior. For instance, n-type *c*P@Cu₃(HHTP)₂ exhibited a higher response during the initial cycle, attributed to its abundant electron concentration facilitating electron donation to NO₂, but this enhanced response rapidly diminished by 78.3% during the second cycle, attributable to the incomplete recovery (or irreversible kinetics) (**Fig. 4 c**). These results effectively emphasize the significance of hole enrichment in the hybrid films enabled by the polymeric component and its effect on the desorption of NO₂ gas, promoting favorable recovery kinetics.

Using density functional theory (DFT) calculations, we also calculated the binding energies between the gas molecules and the sensing material to gain further insight on the effect of *c*P hybridization on the observed sensing behaviors.^[55,56] For our simulations, instead of modeling the entire *c*P@*c*MOFs systems, we represented *c*P@*c*MOFs with p/n-type *c*P as pure *c*MOFs with an additional injected hole/electron. By comparing the hybrid systems with the pure, charge-neutral *c*MOFs, this approach allows us to focus on the hole/electron enrichment effect of *c*Ps on *c*MOFs. For all six *c*MOFs under consideration, our simulations considered three possible metal oxidation states, +0, +1, and +2 on the metal node (**Fig. 4 d** and **Supplementary Fig. 26**). Across all *c*MOFs,

we observed that hole-enriched states exhibit lower binding energy than their neutral state and electron-rich states (**Fig. 4 e**). These simulation results thus further supported our rationale of hole-enrichment as a major contributor to NO₂ desorption and thus sensing reversibility. Note that the case of Co-based *c*MOFs discussed above also show binding energies on par with other *c*MOFs, thus underscoring the importance of other contributing factors to the sensing kinetics such as film crystallinity and crystallite size (**Supplementary Fig. 24 c,d**). We could thus conclude that, in hole-excess scenarios, less electronic charge is transferred from the metal nodes to NO₂, thereby weakening their binding, compared to electron-excess systems (**Fig. 4 b**). This charge transfer between the NO₂ and the metal nodes also supports superior selectivity over other gases, such as H₂S and NH₃, as evidenced by calculated selectivity data in **Supplementary Figs. 22, 27**.

3. Conclusions

In conclusion, we propose a hybridization method combining two complementary classes of mixed ionic-electronic conductors (MIECs), conductive polymers and MOFs (*c*P and *c*MOFs). Our approach produces chemiresistors with better cycling stability and sustained dynamic range than those made solely from *c*MOFs or *c*Ps. We conducted a detailed analysis to understand how hybridization with the conductive polymers enhances the reversibility of *c*MOFs-based sensors, focusing on energy band alignments at the material interfaces and their impact on sensing thermodynamics and binding kinetics. Theoretical calculations further elucidated the effect of such hybridization of the interaction between *c*MOFs and the gaseous analyte. Our approach proves to be versatile towards designing conductive polymer/MOF composites with improved performance and processability. The hybridization thus paves way for more tailored composite-based electronics leveraging the intrinsic properties of both polymers and MOFs.

4. Materials and Methods

Materials

Co(OAc)₂·4H₂O (Alfa Aesar), Co(NO₃)₂·6H₂O (Alfa Aesar), Cu(OAc)₂·xH₂O (Alfa Aesar), CuSO₄·5H₂O (Alfa Aesar), Ni(OAc)₂·4H₂O (Strem), and NaOAc (Alfa Aesar) were used without further purification. 2,3,6,7,10,11-hexaaminotriphenylene hexahydrochloride (HATP·6HCl) was prepared according to a procedure published elsewhere.^[57] 2,3,6,7,10,11-

hexahydroxytriphenylene hydrate (HHTP, $C_{18}H_{12}O_6 \cdot H_2O$, 95%) was purchased from Tokyo Chemical Industry. For the synthesis of HHTP with higher crystallinity, recrystallization of HHTP ligand was conducted. N,N-dimethylformamide (DMF), acetone, and methanol were used as received without further purification. Further synthetic details can be found in Supplementary Information.

cP@cMOF hybrid film processing

A polymer solution of 10 mg/ml in chloroform was prepared and stirred for 30 minutes at 35 °C. The cMOFs were initially dispersed in deionized water and ethanol, for $M_3(\text{HITP})_2$ series and $M_3(\text{HHTP})_2$ series, respectively, immediately after synthesis and filtration. Subsequently, the dispersed cMOFs were sonicated for 5-30 minutes and blended with the polymer solution in appropriate w/w ratio to create the final solution for the hybrid film.

Powder X-ray diffraction (PXRD)

PXRD analysis was conducted using a Bruker Advance II diffractometer equipped with a $\theta/2\theta$ reflection geometry and Ni-filtered Cu $K\alpha$ radiation ($K_{\alpha 1} = 1.5406 \text{ \AA}$, $K_{\alpha 2} = 1.5444 \text{ \AA}$, $K_{\alpha 2}/K_{\alpha 1} = 0.5$). The tube voltage and current were set as 40 kV and 40 mA, respectively, during operation. Samples were prepared by placing the material on a zero-background silicon crystal plate.

Spectroscopy measurements

X-ray photoelectron spectroscopy (XPS) measurements were performed using a Physical Electronics PHI Versaprobe II X-ray photoelectron spectrometer equipped with an Al anode as a source. To prepare the samples for analysis, powders were compressed onto copper tapes to ensure complete coverage. The calibration of charge shift was performed by aligning the C1s peak of surface-adsorbed adventitious carbon to 284.8 eV. Ultraviolet-visible (UV-vis) absorption spectra were acquired using a Perkin Elmer 1050 UV-visible-NIR spectrophotometer. Raman spectra were collected on a Raman Reflex instrument utilizing a 532 nm laser source.

Chemiresistor fabrication and characterization

Gas sensing characterizations involved the coating of sensing materials onto prepatterned Al_2O_3 -based sensor substrates. These substrates featured two parallel electrodes, each measuring 90 μm

in width and spaced 160 μm apart. Following the preparation of the sensing material solutions at a concentration of 10 mg/ml, 5 μl of the solution were cast onto the sensor substrate and dried. Measurement of the resistance of the sensing materials on the electrodes was carried out using a data acquisition system (Agilent 34972A) equipped with a 16-channel multiplexer (Agilent 34902A). For evaluation of sensing characteristics, the measured resistance values were converted into response values ($R_{\text{air}}/R_{\text{gas}}$ or $R_{\text{gas}}/R_{\text{air}}$), where R_{air} and R_{gas} denoted the resistance in air and the gas, respectively. For stabilization of the baseline resistance, a baseline air was employed to stabilize the sensors for at least 2 hours. To establish concentration-dependent measurements, gas cylinders containing 50 ppm NO_2 , 50 ppm H_2S , were purchased from Airgas. These gases were then diluted with air using mass flow controllers. Other organic analytes including ethanol, methanol, acetone, toluene, and xylene, were supplied to the sensing chamber using a FlexStream FlexBase module. Further details regarding sensor fabrication steps and sensor dimensions are provided in Supplementary Information.

Experimental energy level measurement

The electronic band structures were constructed collectively by following measurements: X-ray photoelectron spectroscopy (XPS) with monochromatic Al K α = 1486.6 eV with -10 V bias was conducted to obtain both cut-off and fermi spectra. A gentle ion gun treatment (Monatomic source gun with 2000 eV, 30 seconds etch time) was performed to clean the surface. Tauc plots were converted from UV-vis spectra.

Theoretical calculation details: density functional theory (DFT) calculations

To enable facile control of the charge and oxidation state in our DFT studies, we studied a finite cluster model of the *c*MOF system using the hybrid B3LYP functional and the composite LACVP* basis set. These cluster models were extracted from DFT-optimized structures of the full periodic *c*MOFs with PBE-D2 and a plane wave basis set (kinetic energy cutoff of 400 eV). Full computational details are provided in the Supplementary Information.

Acknowledgements

H.R. and D.-H.K. contributed equally to this work. H. R. and A. G. acknowledge financial support from the MIT Climate & Sustainability Consortium (MCSC) as well as the Abdul Latif Jameel

Water & Food Systems (JWAFS) Lab at the Massachusetts Institute of Technology (MIT). D. H. K. and M. D. acknowledge support from the U.S. Department Of Energy (DE-SC0023288). Y. C. and H. J. K. acknowledge support for the U.S. Department Of Energy (DE-SC0023288) DE-NA0003965.

References

- [1] H. Furukawa, K. E. Cordova, M. O’Keeffe, O. M. Yaghi, *Science*. **2013**, *341*, DOI 10.1126/science.1230444.
- [2] D. Sheberla, J. C. Bachman, J. S. Elias, C. J. Sun, Y. Shao-Horn, M. Dincă, *Nat. Mater.* **2017**, *16*, DOI 10.1038/nmat4766.
- [3] S. Bi, H. Banda, M. Chen, L. Niu, M. Chen, T. Wu, J. Wang, R. Wang, J. Feng, T. Chen, M. Dincă, A. A. Kornyshev, G. Feng, *Nat. Mater.* **2020**, *19*, DOI 10.1038/s41563-019-0598-7.
- [4] A. J. Rieth, A. M. Wright, M. Dincă, *Nat. Rev. Mater.* **2019**, *4*, DOI 10.1038/s41578-019-0140-1.
- [5] W.-T. Koo, J.-S. Jang, I.-D. Kim, *Chem.* **2019**, *5*, DOI 10.1016/j.chempr.2019.04.013.
- [6] X. Chen, R. Behboodiani, D. Bagnall, M. Taheri, N. Nasiri, *Chemosensors* **2021**, *9*, DOI 10.3390/chemosensors9110316.
- [7] L. E. Kreno, K. Leong, O. K. Farha, M. Allendorf, R. P. Van Duyne, J. T. Hupp, *Chem. Rev.* **2012**, *112*, DOI 10.1021/cr200324t.
- [8] B. Lal, K. B. Idrees, H. Xie, C. S. Smoljan, S. Shafaie, T. Islamoglu, O. K. Farha, *Angew. Chem. Int. Ed.* **2023**, *62*, DOI 10.1002/anie.202219053.
- [9] Y. K. Jo, S. Y. Jeong, Y. K. Moon, Y. M. Jo, J. W. Yoon, J. H. Lee, *Nat. Commun.* **2021**, *12*, DOI 10.1038/s41467-021-25290-3.
- [10] M. Eddaoudi, J. Kim, N. Rosi, D. Vodak, J. Wachter, M. O’Keeffe, O. M. Yaghi, *Science*. **2002**, *295*, DOI 10.1126/science.1067208.
- [11] M. G. Campbell, S. F. Liu, T. M. Swager, M. Dincă, *J. Am. Chem. Soc.* **2015**, *137*, 13780. DOI 10.1021/jacs.5b09600.
- [12] M. G. Campbell, D. Sheberla, S. F. Liu, T. M. Swager, M. Dincă, *Angew. Chem. Int. Ed.* **2015**, *54*, DOI 10.1002/anie.201411854.
- [13] H. Thakkar, S. Eastman, Q. Al-Naddaf, A. A. Rownaghi, F. Rezaei, *ACS Appl. Mater. Interfaces* **2017**, *9*, DOI 10.1021/acsami.7b11626.

- [14] R. Zhang, S. Ji, N. Wang, L. Wang, G. Zhang, J. R. Li, *Angew. Chem. Int. Ed.* **2014**, *53*, DOI 10.1002/anie.201403978.
- [15] Y. Lei, Y. Sun, H. Zhang, L. Liao, S. T. Lee, W. Y. Wong, *Chem. Commun.* **2016**, *52*, DOI 10.1039/c6cc06456f.
- [16] L. G. S. Albano, D. H. S. de Camargo, G. R. Schleder, S. G. Deeke, T. P. Vello, L. D. Palermo, C. C. Corrêa, A. Fazzio, C. Wöll, C. C. B. Bufon, *Small.* **2021**, *17*, 2101475. DOI 10.1002/sml.202101475.
- [17] R. M. L. da Silva, L. G. S. Albano, T. P. Vello, W. W. R. de Araújo, D. H. S. de Camargo, L. D. Palermo, C. C. Corrêa, C. Wöll, C. C. B. Bufon, *Adv. Electron. Mater.* **2022**, *8*, 2200175. DOI 10.1002/aelm.202200175.
- [18] Y. Liu, Y. Wei, M. Liu, Y. Bai, X. Wang, S. Shang, C. Du, W. Gao, J. Chen, Y. Liu, *Adv. Mater.* **2021**, *33*, 2007741. DOI 10.1002/adma.202007741.
- [19] C. Park, W. T. Koo, S. Chong, H. Shin, Y. H. Kim, H. J. Cho, J. S. Jang, D. H. Kim, J. Lee, S. Park, J. Ko, J. Kim, I. D. Kim, *Adv. Mater.* **2021**, *33*, 2101216. DOI 10.1002/adma.202101216.
- [20] C. K. Liu, V. Piradi, J. Song, Z. Wang, L. W. Wong, E. H. L. Tan, J. Zhao, X. Zhu, F. Yan, *Adv. Mater.* **2022**, *34*, 2204140. DOI 10.1002/adma.202204140.
- [21] Y. M. Jo, K. Lim, J. W. Yoon, Y. K. Jo, Y. K. Moon, H. W. Jang, J. H. Lee, *ACS Cent. Sci.* **2021**, *7*, 1176–1182. DOI 10.1021/acscentsci.1c00289.
- [22] W. T. Koo, S. J. Kim, J. S. Jang, D. H. Kim, I. D. Kim, *Adv. Sci.* **2019**, *6*, DOI 10.1002/advs.201900250.
- [23] M.-S. Yao, X.-J. Lv, Z.-H. Fu, W.-H. Li, W.-H. Deng, G.-D. Wu, G. Xu, *Angew. Chem. Int. Ed.* **2017**, *56*, 16510. DOI 10.1002/anie.201709558.
- [24] Y.-M. Jo, Y. K. Jo, J.-H. Lee, H. W. Jang, I.-S. Hwang, D. J. Yoo, *Adv. Mater.* **2023**, *35*, 2206842. DOI 10.1002/adma.202206842.
- [25] Y. Lin, W.-H. Li, Y. Wen, G.-E. Wang, X.-L. Ye, G. Xu, *Angew. Chem. Int. Ed.* **2021**, *60*, 25758. DOI 10.1002/anie.202111519.
- [26] J.-O. Kim, W.-T. Koo, H. Kim, C. Park, T. Lee, C. A. Hutomo, S. Q. Choi, D. S. Kim, I.-D. Kim, S. Park, *Nat. Commun.* **2021**, *12*, 4294. DOI 10.1038/s41467-021-24571-1.
- [27] A. M. Wright, C. Sun, M. Dincă, *J. Am. Chem. Soc.* **2021**, *143*, DOI 10.1021/jacs.0c12134.
- [28] A. J. Timmons, M. D. Symes, *Chem. Soc. Rev.* **2015**, *44*, DOI 10.1039/c5cs00269a.

- [29] H. Z. Li, Y. Pan, Q. Li, Q. Lin, D. Lin, F. Wang, G. Xu, J. Zhang, *J. Mater. Chem. A Mater.* **2022**, *11*, DOI 10.1039/d2ta08921a.
- [30] M. G. Campbell, S. F. Liu, T. M. Swager, M. Dincă, *J. Am. Chem. Soc.* **2015**, *137*, 13780. DOI 10.1021/jacs.5b09600.
- [31] C. M. Amb, A. L. Dyer, J. R. Reynolds, C. M. Amb, A. L. Dyer, J. R. Reynolds, *Chem. Mater.* **2011**, *23*, 397.
- [32] C. M. Amb, P. M. Beaujuge, J. R. Reynolds, *Adv. Mater.* **2010**, *22*, DOI 10.1002/adma.200902917.
- [33] H. Roh, S. Yue, H. Hu, K. Chen, H. J. Kulik, A. Gumyusenge, *Adv. Funct. Mater.* **2023**, DOI 10.1002/adfm.202304893.
- [34] H. Chae, J. M. Han, Y. Ahn, J. E. Kwon, W. H. Lee, B.-G. Kim, *Adv. Mater. Technol.* **2021**, *6*, 2100580. DOI 10.1002/admt.202100580.
- [35] Y. Kang, D. H. Kwak, J. E. Kwon, B.-G. Kim, W. H. Lee, *ACS Appl. Mater. Interfaces* **2021**, *13*, 31910-31918. DOI 10.1021/acsami.1c05681.
- [36] S. T. Navale, A. T. Mane, G. D. Khuspe, M. A. Chougule, V. B. Patil, *Synth. Met.* **2014**, *195*, 228. DOI 10.1016/j.orgel.2014.06.019.
- [37] G. G. Yang, D.-H. Kim, S. Samal, J. Choi, H. Roh, C. E. Cunin, H. M. Lee, S. O. Kim, M. Dincă, A. Gumyusenge, *ACS Sens.* **2023**, *8*, 3687.
- [38] R. M. Stolz, A. Mahdavi-Shakib, B. G. Frederick, K. A. Mirica, *Chem. Mater.* **2020**, *32*, DOI 10.1021/acs.chemmater.0c01007.
- [39] S. T. Navale, A. T. Mane, M. A. Chougule, R. D. Sakhare, S. R. Nalage, V. B. Patil, *Synth. Met.* **2014**, *189*, DOI 10.1016/j.synthmet.2014.01.002.
- [40] S. T. Navale, A. T. Mane, G. D. Khuspe, M. A. Chougule, V. B. Patil, *Synth. Met.* **2014**, *195*, DOI 10.1016/j.synthmet.2014.06.017.
- [41] X. B. Yan, Z. J. Han, Y. Yang, B. K. Tay, *Sens. Actuators B Chem.* **2007**, *123*, DOI 10.1016/j.snb.2006.07.031.
- [42] R. K. Sonker, B. C. Yadav, G. I. Dzhardimalieva, *J. Inorg. Organomet. Polym. Mater.* **2016**, *26*, DOI 10.1007/s10904-016-0439-y.
- [43] N. Karmakar, R. Fernandes, S. Jain, U. V. Patil, N. G. Shimpi, N. V. Bhat, D. C. Kothari, *Sens. Actuators B Chem.* **2017**, *242*, DOI 10.1016/j.snb.2016.11.039.

- [44] Y. Zhang, J. J. Kim, D. Chen, H. L. Tuller, G. C. Rutledge, *Adv. Funct. Mater.* **2014**, *24*, DOI 10.1002/adfm.201400185.
- [45] Q. Y. Zheng, M. Yang, X. Dong, X. F. Zhang, X. L. Cheng, L. H. Huo, Z. Major, Y. M. Xu, *Rare Metals* **2023**, *42*, DOI 10.1007/s12598-022-02149-0.
- [46] A. T. Mane, S. T. Navale, V. B. Patil, *Org. Electron.* **2015**, *19*, DOI 10.1016/j.orgel.2015.01.018.
- [47] S. T. Navale, G. D. Khuspe, M. A. Chougule, V. B. Patil, *Ceram. Int.* **2014**, *40*, DOI 10.1016/j.ceramint.2013.12.153.
- [48] H. Park, D. H. Kim, B. S. Ma, E. Shin, Y. Kim, T. S. Kim, F. S. Kim, I. D. Kim, B. J. Kim, *Adv. Sci.* **2022**, *9*, DOI 10.1002/advs.202200270.
- [49] J. O. Kim, W. T. Koo, H. Kim, C. Park, T. Lee, C. A. Hutomo, S. Q. Choi, D. S. Kim, I. D. Kim, S. Park, *Nat. Commun.* **2021**, *12*, DOI 10.1038/s41467-021-24571-1.
- [50] X. Su, Z. Zhong, X. Yan, T. Zhang, C. Wang, Y. X. Wang, G. Xu, L. Chen, *Angew. Chem. Int. Ed.* **2023**, *62*, DOI 10.1002/anie.202302645.
- [51] G. Grosso, G. P. Parravicini, *Solid State Physics (2nd Edition)*, **2014**. DOI 10.1016/C2010-0-66724-1.
- [52] Z. Yin, M. Tordjman, Y. Lee, A. Vardi, R. Kalish, J. A. Del Alamo, *Sci. Adv.* **2018**, *4*, DOI 10.1126/sciadv.aau0480.
- [53] C. Y. Lee, M. S. Strano, *Langmuir* **2005**, *21*, DOI 10.1021/la046867i.
- [54] D.-H. Kim, S. Chong, C. Park, J. Ahn, J.-S. Jang, J. Kim, I.-D. Kim, *Adv. Mater.* **2022**, *34*, 2105869. DOI 10.1002/adma.202105869.
- [55] K. W. Nam, S. S. Park, R. dos Reis, V. P. Dravid, H. Kim, C. A. Mirkin, J. F. Stoddart, *Nat. Commun.* **2019**, *10*, DOI 10.1038/s41467-019-12857-4.
- [56] M. E. Foster, K. Sohlberg, C. D. Spataru, M. D. Allendorf, *J. Phys. Chem. C.* **2016**, *120*, DOI 10.1021/acs.jpcc.6b05746.
- [57] T. Chen, J.H. Dou, L. Yang, C. Sun, N.J. Libretto, G. Skorupskii, J.T. Miller, M. Dincă, Continuous electrical conductivity variation in M₃(hexaiminotriphenylene)₂ (M= Co, Ni, Cu) MOF alloys. *J. Am. Chem. Soc.* **2020**, *142*, 12367. DOI 10.1021/jacs.0c04458.

Supporting Information

Robust Chemiresistive Behavior in Conductive Polymer/MOF Composites

Heejung Roh, Dong-Ha Kim, Yeongsu Cho, Young-Moo Jo, Jesús A. del Alamo, Heather J.

*Kulik, *Mircea Dincă, * Aristide Gumyusenge **

Table of Contents

- 1) **Synthetic Details**
- 2) **Density Functional Theory (DFT) Calculations Details**
- 3) **Supplementary Figures and Tables**
- 4) **Supplementary References**

1) Synthetic Details

Synthesis of $\text{Co}_3(\text{HHTP})_2$

20 mg of $\text{Co}(\text{OAc})_2 \cdot 4\text{H}_2\text{O}$ was dispersed in 4 ml of water. Then, 16.2 mg of recrystallized HHTP ligand was dispersed in the mixture of 4 ml of water and 2 ml of DMF solvents. After mixing of the two solutions, sonication was conducted for 5 minutes. Then, the mixed solution was put into the sand heated at 85 °C for 24 hours (vial closed, without stirring). After reaction, the solution was filtered and washed with a large amount of water and acetone. Then, the obtained powder was dried overnight. Note that for the synthesis of $\text{Co}_3(\text{HHTP})_2$ with higher crystallinity, 16.2 mg of recrystallized HHTP ligand was dispersed in the mixture of 1.33 ml of water and 0.67 ml of DMF solvents. All the other synthetic procedures remain unchanged.

Synthesis of $\text{Cu}_3(\text{HHTP})_2$

24.9 mg of $\text{Cu}(\text{OAc})_2 \cdot \text{H}_2\text{O}$ was dispersed in 4 ml of water. 16.2 mg of recrystallized HHTP ligand was dispersed in 4 ml of DMF solvent. After mixing of the solutions, sonication was conducted for 5 minutes. Then, the mixed solution was put into the sand heated at 85 °C for 24 hours (vial closed, without stirring). After reaction, the solution was filtered and washed with a large amount of water and acetone. Then, the obtained powder was dried overnight. For the synthesis of $\text{Cu}_3(\text{HHTP})_2$ with lower crystallinity, commercial HHTP ligand (without recrystallization process) was utilized with the same synthetic protocols.

Synthesis of $\text{Ni}_3(\text{HHTP})_2$

24.9 mg of $\text{Ni}(\text{OAc})_2 \cdot 4\text{H}_2\text{O}$ was dispersed in 4 ml of water. 16.2 mg of recrystallized HHTP ligand was dispersed in 4 ml of water. After mixing the solutions, sonication was conducted for 5 minutes. Then, the mixed solution was put into the sand heated at 85 °C for 24 hours (vial closed, without stirring). After reaction, the solution was filtered and washed with a large amount of water and acetone. Then, the obtained powder was dried overnight.

Synthesis of $\text{Co}_3(\text{HITP})_2$

8.13 mg of $\text{Co}(\text{NO}_3)_2 \cdot 6\text{H}_2\text{O}$ was dispersed in 3 ml of DMF. 10 mg of $\text{HATP} \cdot 6\text{HCl}$ ligand was dispersed in 3 ml of water. After mixing the solutions, sonication was conducted for 5 minutes. Then, 4 ml of 2M NaOAc was added to the solution and the mixed solution was put into the sand

heated at 65 °C for 2 hours (vial opened, with stirring). After reaction, the solution was filtered and washed with a large amount of water and methanol. Then, the obtained powder was dried overnight.

Synthesis of Cu₃(HITP)₂

7 mg of Cu(SO₄)₂·5H₂O was dispersed in 3 ml of DMF. 10 mg of HATP·6HCl ligand was dispersed in 3 ml of water. The mixed solution was sonicated for 5 minutes and put into the sand heated at 65 °C. Then, 4 ml of 2M NaOAc was added to the solution and heated at 65 °C for 2 hours (vial opened, with stirring). After reaction, the solution was filtered and washed with a large amount of water and methanol. Then, the obtained powder was dried overnight.

Synthesis of Ni₃(HITP)₂

6.94 mg of Ni(OAc)₂·4H₂O was dispersed in 3 ml of DMF. 10 mg of HATP·6HCl ligand was dispersed in 3 ml of water. The mixed solution was sonicated for 5 minutes and put into the sand heated at 65 °C. Then, 8 ml of 2M NaOAc was added to the solution and heated at 65 °C for 2 hours (vial opened, with stirring). After reaction, the solution was filtered and washed with a large amount of water and methanol. Then, the obtained powder was dried overnight.

Synthesis of P-type cP

P-type cP selected for this study consists of ProDOT and BTB building units according to the previous reported procedure¹.

Synthesis of N-type cP

N-type cP selected for this study is N2200, or PNDI-2T, or Poly{[N,N'-bis(2-octyldodecyl)-naphthalene-1,4,5,8-bis(dicarboximide)-2,6-diyl]-alt-5,5'-(2,2'-bithiophene)}² was synthesized using a Pd-catalyzed Stille coupling reaction. NDI-Br₂ (0.50 g, 0.46 mmol) and 5,5'-bis(trimethylstannyl)-2,2'-bithiophene (0.226 g, 0.46 mmol) were dissolved in dry chlorobenzene (7.5 mL). After degassing with N₂ for 1 h, Pd₂(dba)₃ (8 mg) and P(o-Tol)₃ (11 mg) were added to the mixture and stirred for 48 h at 110 °C. Subsequently, 2-bromothiophene and tributyl(thiophen-2-yl)stannane were injected to the reaction mixture for end-capping, and the reaction was stirred for 6 h. The polymer was precipitated in methanol, collected by filtration, and then purified by

successive Soxhlet extraction with methanol, acetone, hexane, toluene, and chloroform. The final product was obtained by precipitation in methanol.

2) Density Functional Theory (DFT) Calculations Details

Our starting structure was based on the experimentally determined lattice parameters of $\text{Cu}_3(\text{HHTP})_2$ as reported in reference 1³. Each unit cell includes two layers, which were offset by a fractional coordinate of (1/32, 0, 0), following reference 2⁴ (**Supplementary Fig. 25a,b**). The atomic positions and lattice parameters were optimized using the Vienna Ab Initio Simulation Package (VASP) version 6.3.1⁵⁻⁸, until the total energy converged to within 0.01 eV. We employed the Perdew-Burke-Ernzerhof (PBE) functional⁷ along with the plane-augmented wave (PAW) pseudopotential¹⁰. A kinetic energy cutoff of 400 eV was used, and DFT-D2 corrections were applied to account for dispersion interactions⁹. Given the large size of the unit cell, calculations were performed at the Γ point only. A background charge of +12 per unit cell was applied to the system. Additionally, each metal atom was assumed to have an oxidation state of +2 and to be in a high-spin state with ferromagnetic ordering.

DFT calculations for the *c*MOF cluster and the monomer of *c*P were performed using TeraChem¹². The B3LYP functional¹³⁻¹⁵ was used with the LACVP* basis set, which consists of 6-31G* for elements ranging from H to Ar, and employs the LANL2DZ effective core potential for heavier atoms¹⁶. To obtain the *c*MOF cluster, one metal node and two linker molecules were extracted from the optimized full MOF structure. Subsequently, hydrogen atoms were added to the truncated bonds, and the positions of the hydrogen atoms were optimized. For calculating the binding energy of the gas molecules, we optimized the positions of the gas molecules while keeping the atomic positions of the *c*MOF cluster fixed. The L-BFGS algorithm was utilized for geometry optimizations via the translation-rotation-internal coordinate optimizer^{17,18}. We considered three different metal oxidation states, +0, +1, and +2, each in high spin state. The oxidation state of the metal atom was adjusted by varying the number of hydrogen atoms on the metal-coordinating oxygen atoms, rather than by altering the system's total charge, to neutralize the metal node (**Supplementary Fig. 25c-e**). This approach was taken because excess negative charge around the metal atom would ionize NO_2 to NO_2^- and simply repel away the ion during the structure optimization. Overall charge neutrality was maintained, except for the hole-excess and electron-

excess *c*MOF systems which were simulated by removing or adding one electron to the *c*MOF cluster, respectively. To model adsorption, we assumed that H₂S and NH₃ adsorbed via the sulfur and nitrogen atoms, respectively, while both N-binding and O-binding were considered as possible adsorbate orientations for NO₂ (**Supplementary Fig. 25f-i**). Likewise, the structure of the *cP* monomer was optimized, and the binding energies of the gas molecules were determined by optimizing their positions while fixing the atomic coordinates of the monomer. A negative binding energy indicates favorable binding.

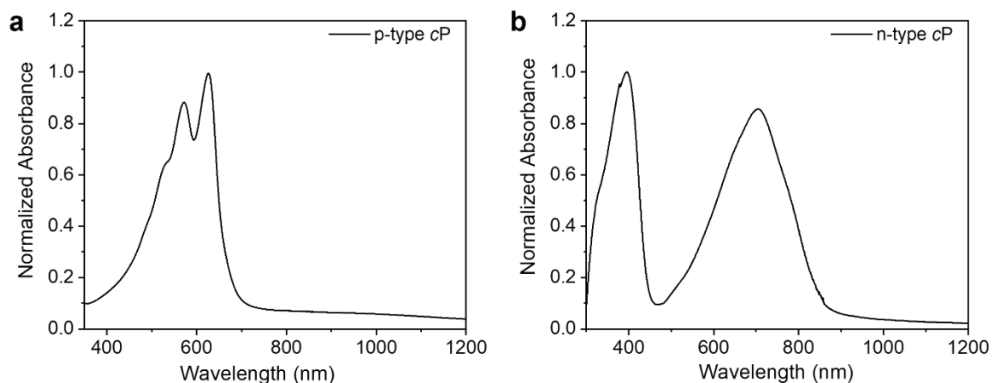
H₂S, NH₃, and NO₂ selectivity

We compared the binding energies of H₂S, NH₃, and NO₂ to investigate the source of NO₂ selectivity. Across all MOFs of all oxidation states, NO₂ generally exhibits stronger binding than H₂S or NH₃ (**Supplementary Fig. 26**). Out of 36 total cases, only five exceptions to this trend were observed, specifically in cases involving Ni₃(HHTP)₂ and Cu₃(HHTP)₂. Furthermore, the binding energy of NO₂, considering both N-binding and O-binding, ranges from -3.3 to -0.2 eV, whereas the binding energies of H₂S and NH₃ never exceed -1.0 eV. The notable disparity in the range of binding energies suggests that the primary interaction between the metal node and H₂S or NH₃ is largely governed by van der Waals interactions, unlike NO₂ binding which is enhanced by chemisorption.

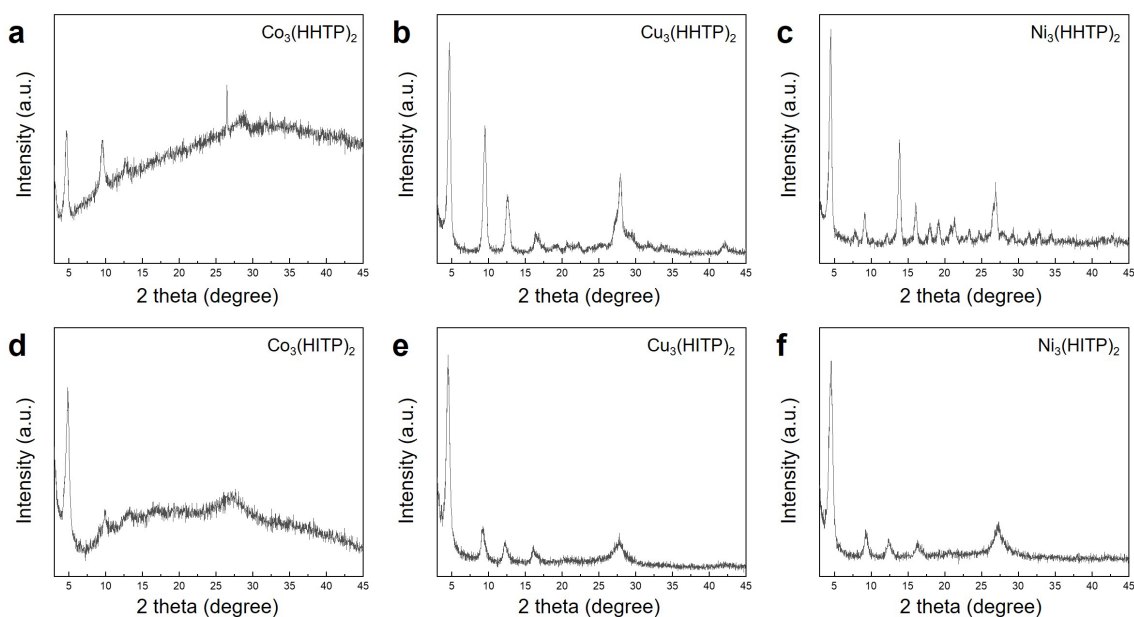
Gas molecule adsorption on *cP*

We assessed the binding energies of gas molecules with the *cP* to determine whether the primary adsorption site is the *cP* or *c*MOF. We modeled ProDOT connected to BTM as a monomer and considered eight potential adsorption sites that were neither carbon nor hydrogen atoms. The binding energies of all three gas molecules fell within a range of -0.20 to -0.05 eV, suggesting that the interactions between the *cP* and the gas molecules are primarily weak van der Waals interactions (**Supplementary Fig. 21**). The gas molecules exhibited stronger binding with the *c*MOF than with the *cP*, indicating that the primary adsorption site is likely the metal node of the *c*MOF.

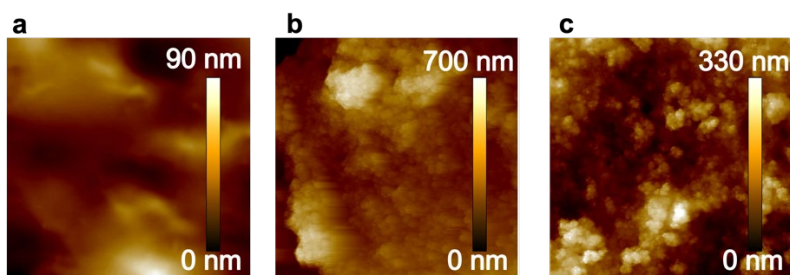
3) Supplementary Figures and Tables



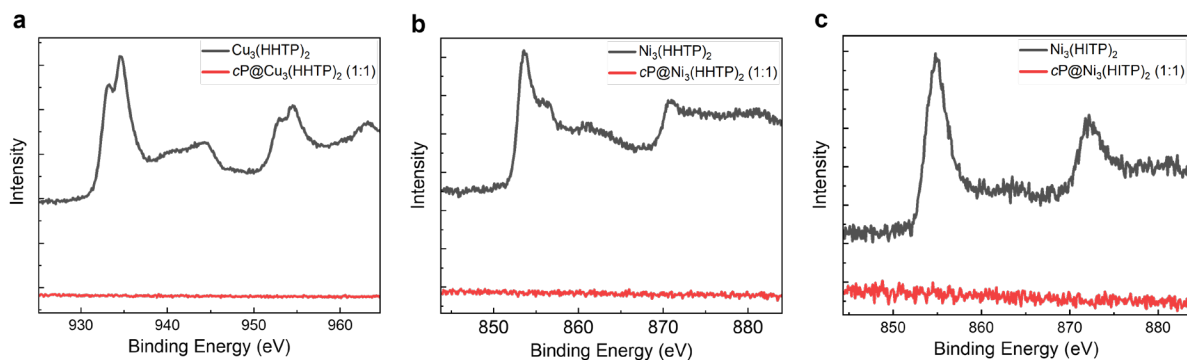
Supplementary Fig. 1 | UV-vis spectra of p-type cP and n-type cP.



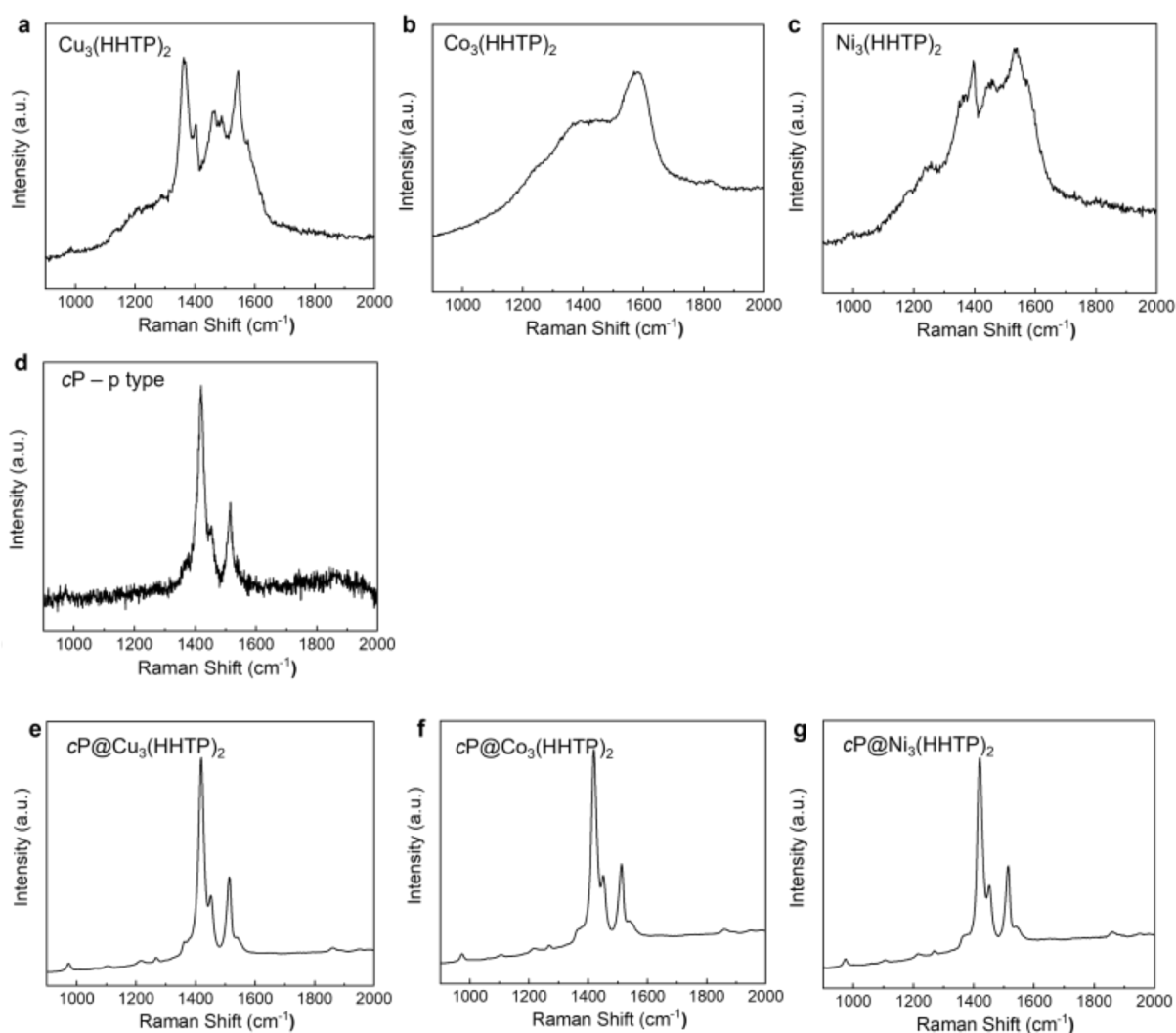
Supplementary Fig. 2 | XRD analysis of **a**, $\text{Co}_3(\text{HHTP})_2$, **b**, $\text{Cu}_3(\text{HHTP})_2$, **c**, $\text{Ni}_3(\text{HHTP})_2$, **d**, $\text{Co}_3(\text{HITP})_2$, **e**, $\text{Cu}_3(\text{HITP})_2$, and **f**, $\text{Ni}_3(\text{HITP})_2$.



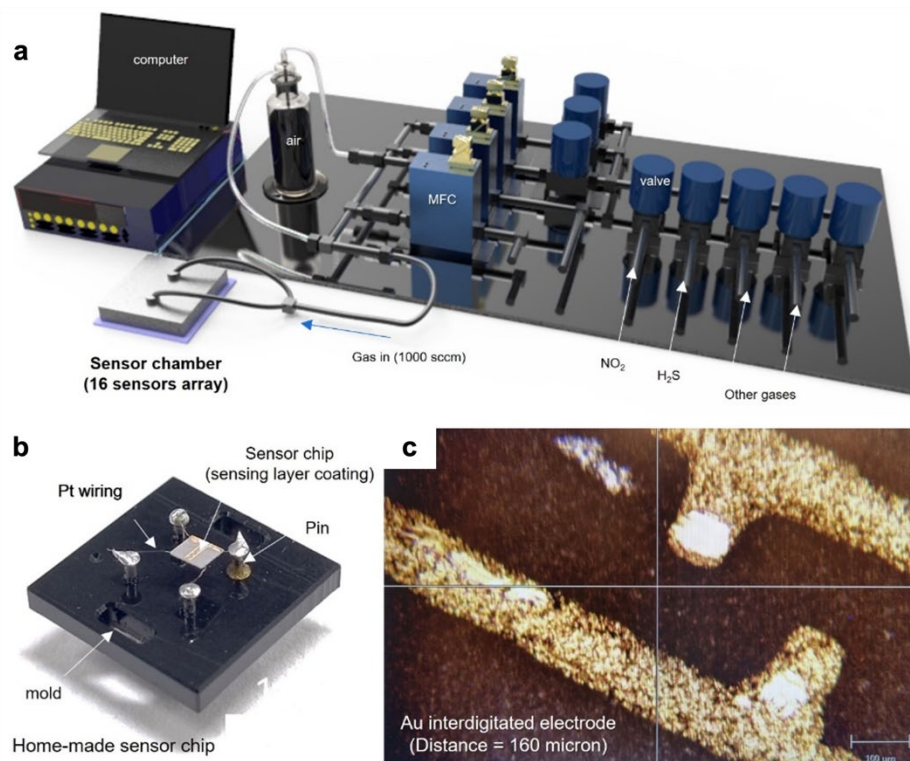
Supplementary Fig. 3 | Atomic force microscopy (AFM) images were obtained for a $5 \mu\text{m} \times 5 \mu\text{m}$ area and corresponding film roughness parameter (Rq) were determined as 22.7 nm, 195 nm, and 97.5 nm for **a**, cP, **b**, cMOF, and **c**, cP@cMOF, respectively.



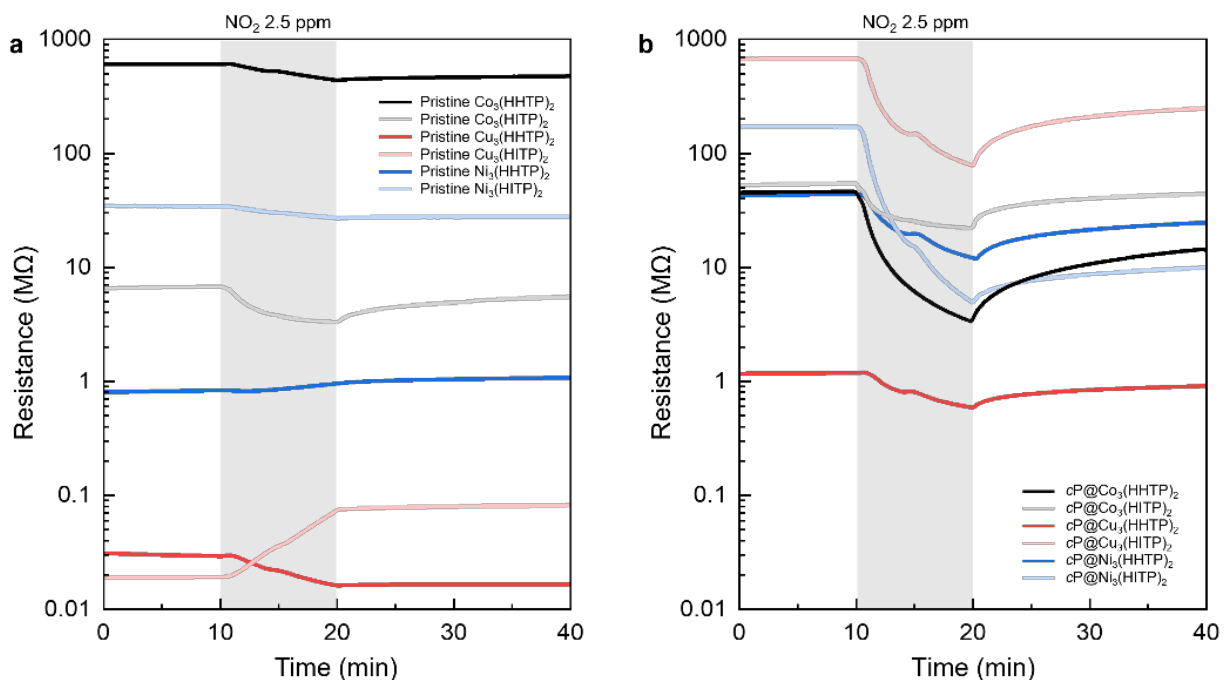
Supplementary Fig. 4 | High-resolution XPS spectra of pristine *c*MOFs and *cP@c*MOFs hybrids (1:1 w/w% if not mentioned otherwise) using **a**, Cu₃(HHTP)₂, **b**, Ni₃(HHTP)₂ and **c**, Ni₃(HITP)₂-based *c*MOFs, respectively.



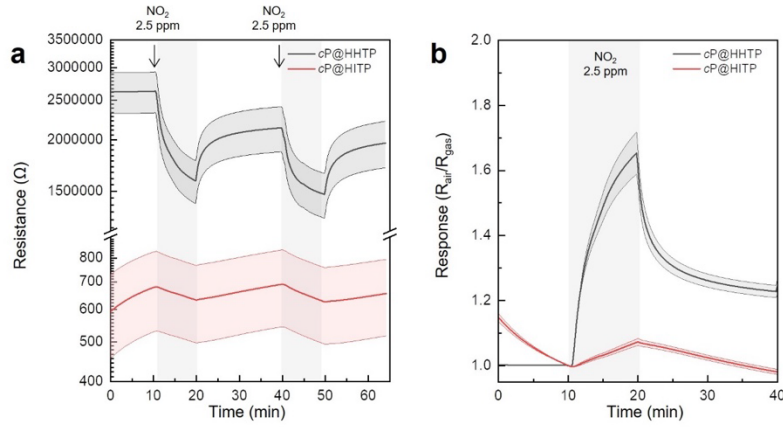
Supplementary Fig. 5 | Raman spectra of **a-c**, pristine *c*MOFs, **d**, pristine *cP*, and **e-g**, corresponding hybrid *cP@c*MOF (1:1).



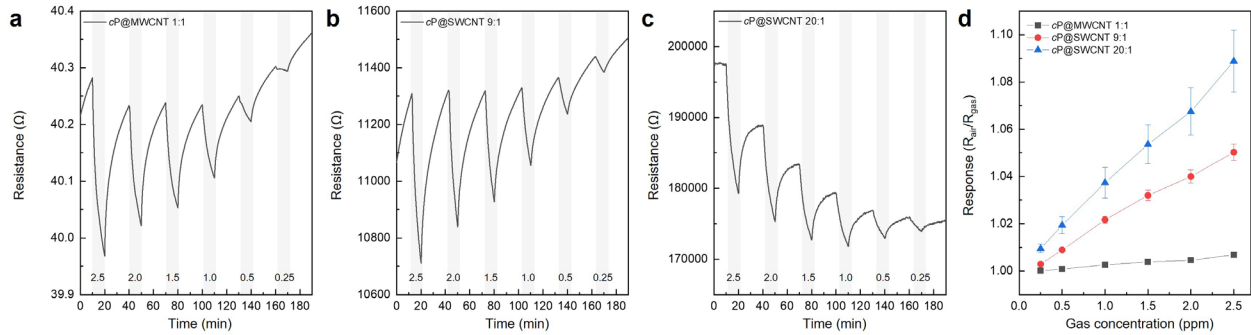
Supplementary Fig. 6 | **a**, Schematic illustrations of the lab-made gas sensing measurement systems. Optical images of the **b**, sensor chip and **c**, sensor electrode.



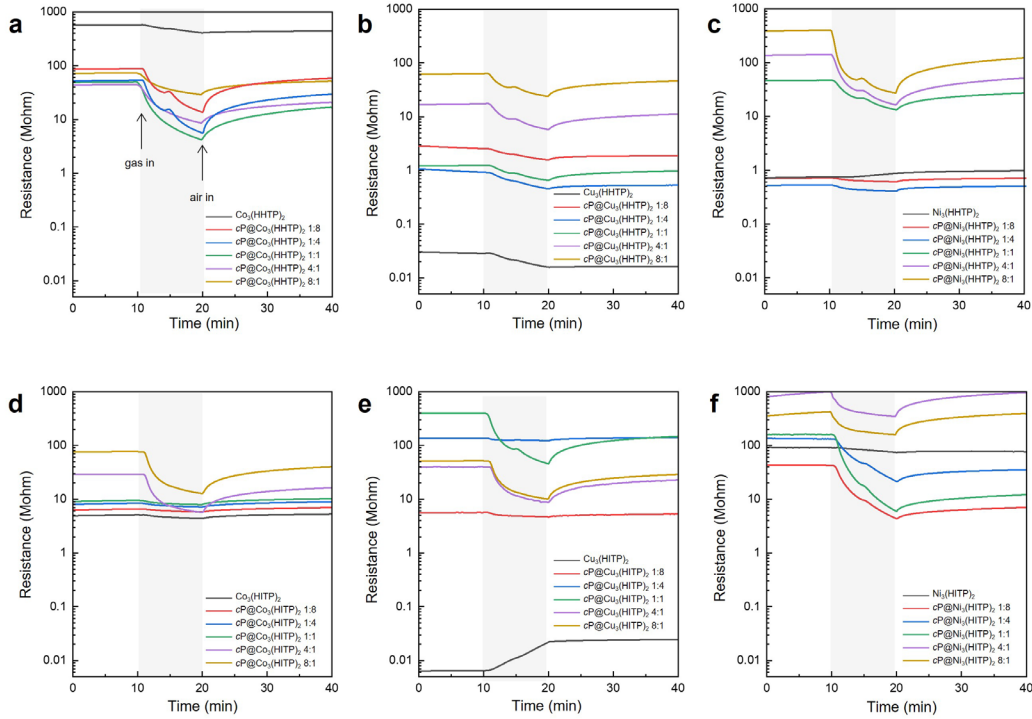
Supplementary Fig. 7 | Resistance transitions of **a**, pristine $cMOFs$ and **b**, $cP@cMOFs$ (1:1) toward 2.5 ppm NO_2 gas.



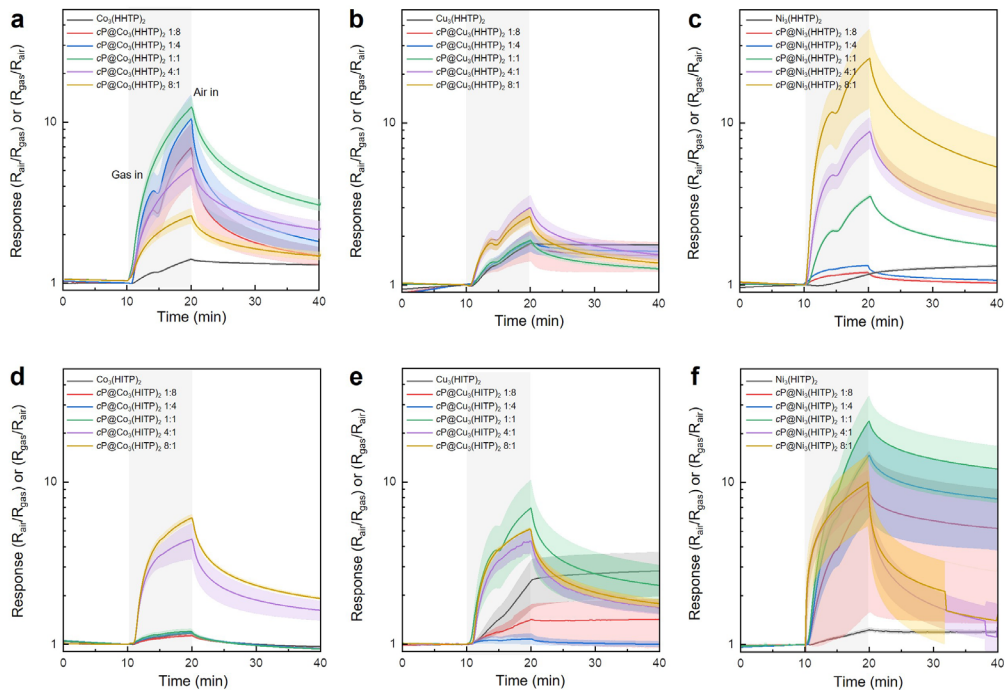
Supplementary Fig. 8 | **a**, Dynamic resistance transitions and **b**, the corresponding response graphs of cP@HHTP and cP@HITP upon exposure to NO₂ gas (N = 3).



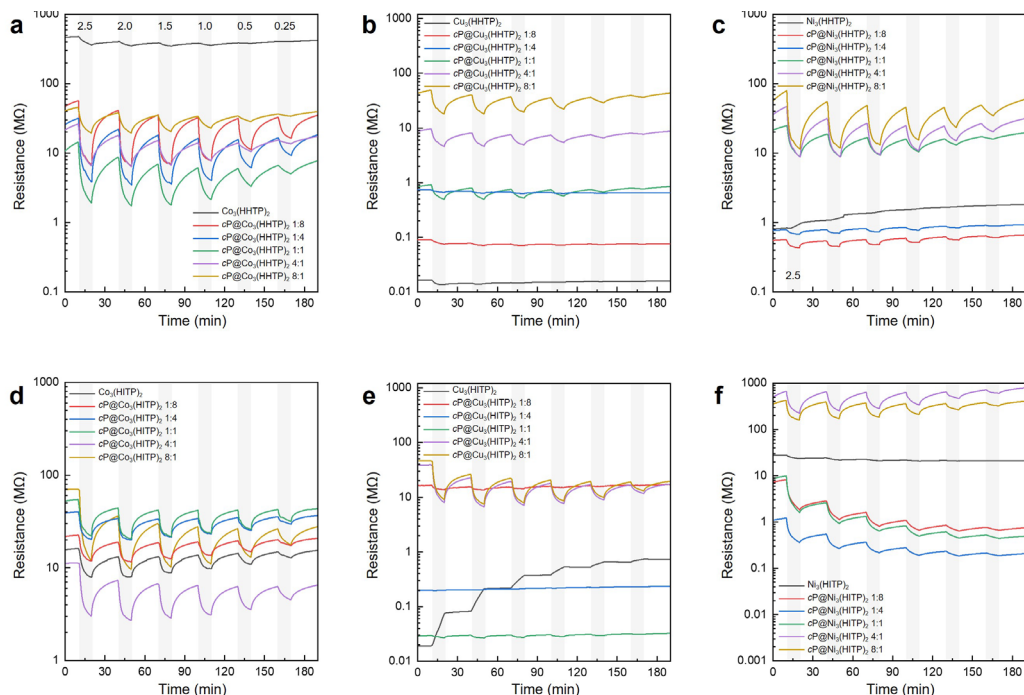
Supplementary Fig. 9 | Dynamic resistance transitions of **a**, cP@MWCNT 1:1 w/w %, **b**, cP@SWCNT 9:1 w/w %, and **c**, cP@SWCNT 20:1 w/w % upon exposure to 2.5-0.25 ppm NO₂ gas. **d**, The corresponding response graph (N = 3).



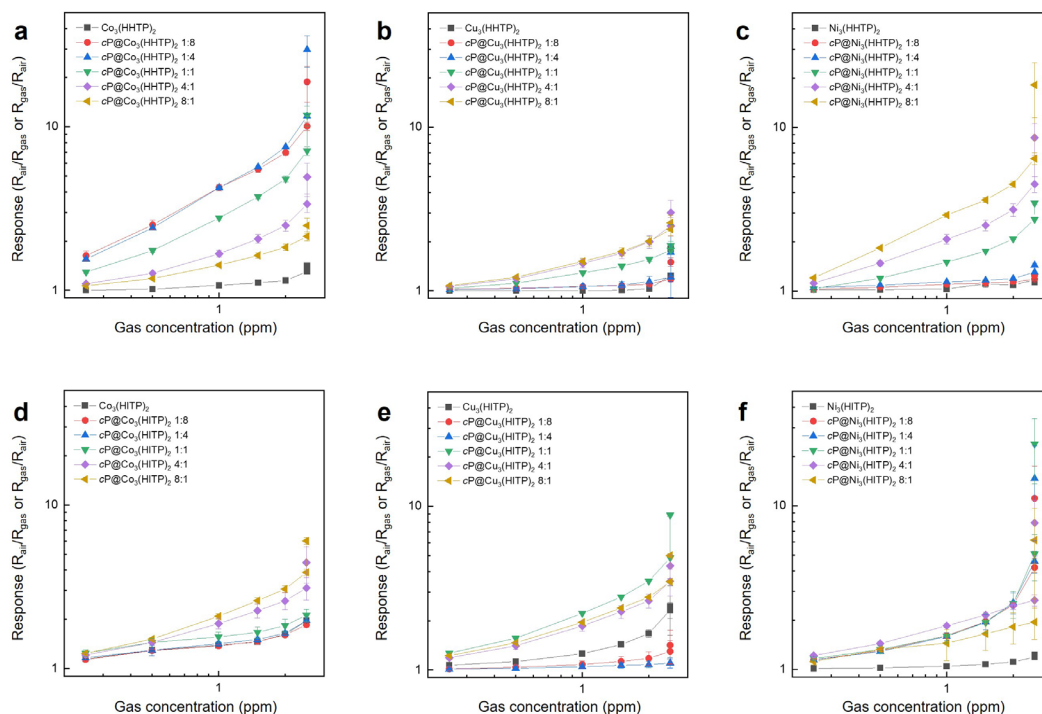
Supplementary Fig. 10 | Dynamic resistance transitions of pristine *c*MOFs and *cP@c*MOFs toward 2.5 ppm NO₂ gas. **a**, Co₃(HHTP)₂, **b**, Cu₃(HHTP)₂, **c**, Ni₃(HHTP)₂, **d**, Co₃(HITP)₂, **e**, Cu₃(HITP)₂, and **f**, Ni₃(HITP)₂-based sensors with various ratios between *cP* and *c*MOFs.



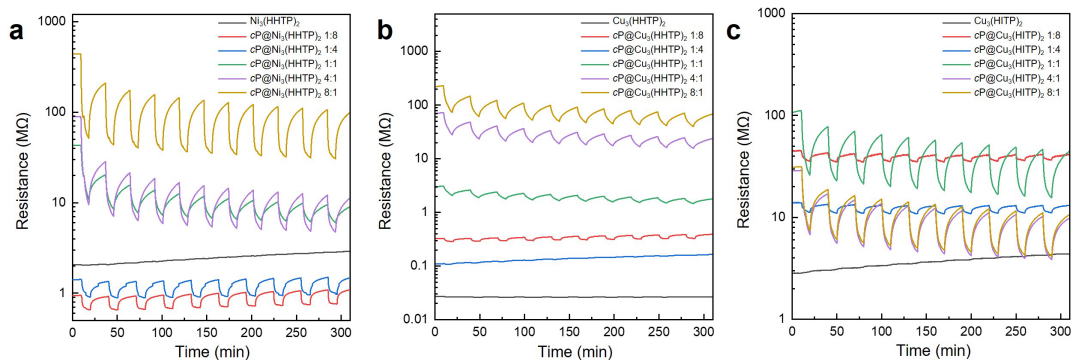
Supplementary Fig. 11 | Response graphs of pristine *c*MOFs and *cP@c*MOFs. **a**, Co₃(HHTP)₂, **b**, Cu₃(HHTP)₂, **c**, Ni₃(HHTP)₂, **d**, Co₃(HITP)₂, **e**, Cu₃(HITP)₂, and **f**, Ni₃(HITP)₂-based sensors with various ratios between *cP* and *c*MOFs ($N \geq 3$).



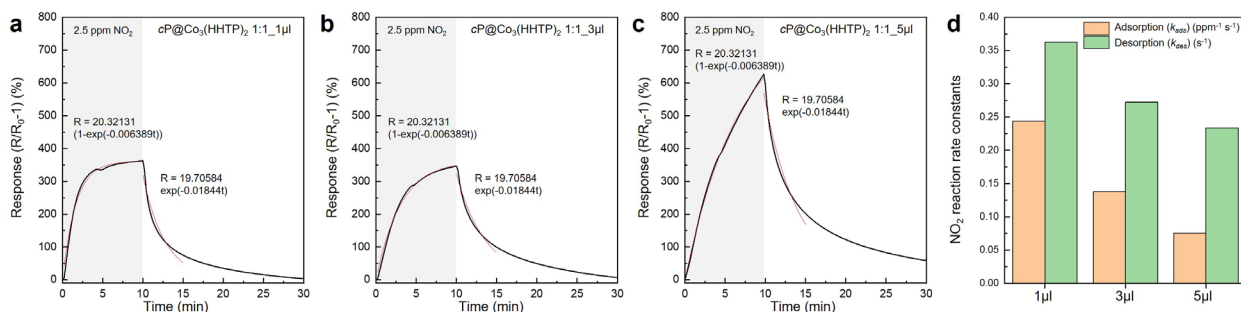
Supplementary Fig. 12 | Dynamic resistance transitions of pristine *c*MOFs and *cP@c*MOFs toward 2.5-0.25 ppm NO_2 gas. **a**, $\text{Co}_3(\text{HHTP})_2$, **b**, $\text{Cu}_3(\text{HHTP})_2$, **c**, $\text{Ni}_3(\text{HHTP})_2$, **d**, $\text{Co}_3(\text{HITP})_2$, **e**, $\text{Cu}_3(\text{HITP})_2$, and **f**, $\text{Ni}_3(\text{HITP})_2$ -based sensors with various ratios between *cP* and *c*MOFs.



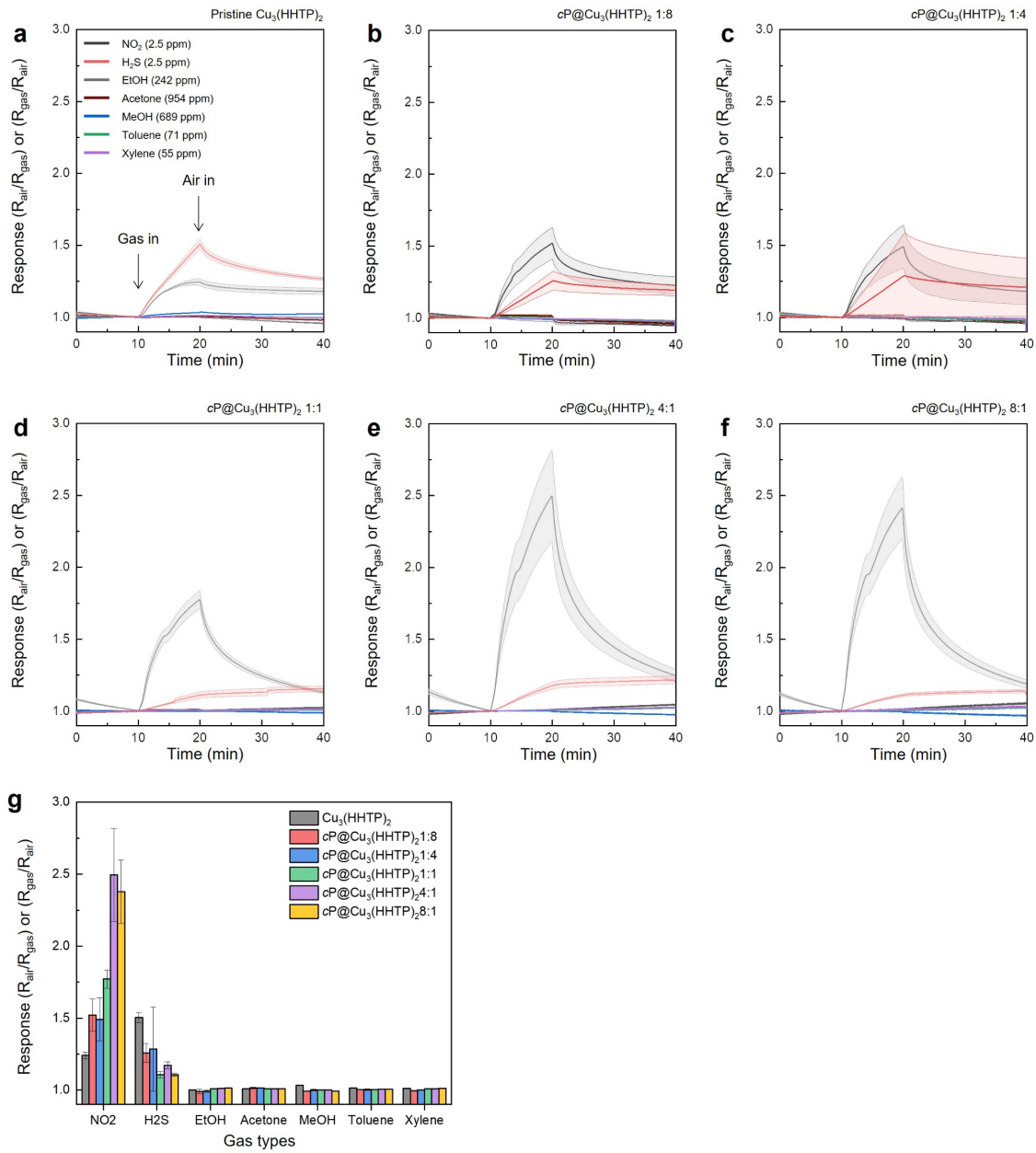
Supplementary Fig. 13 | Response graphs of pristine *c*MOFs and *cP@c*MOFs toward 2.5-0.25 ppm NO_2 gas. **a**, $\text{Co}_3(\text{HHTP})_2$, **b**, $\text{Cu}_3(\text{HHTP})_2$, **c**, $\text{Ni}_3(\text{HHTP})_2$, **d**, $\text{Co}_3(\text{HITP})_2$, **e**, $\text{Cu}_3(\text{HITP})_2$, and **f**, $\text{Ni}_3(\text{HITP})_2$ -based sensors with various ratios between *cP* and *c*MOFs ($N \geq 3$).



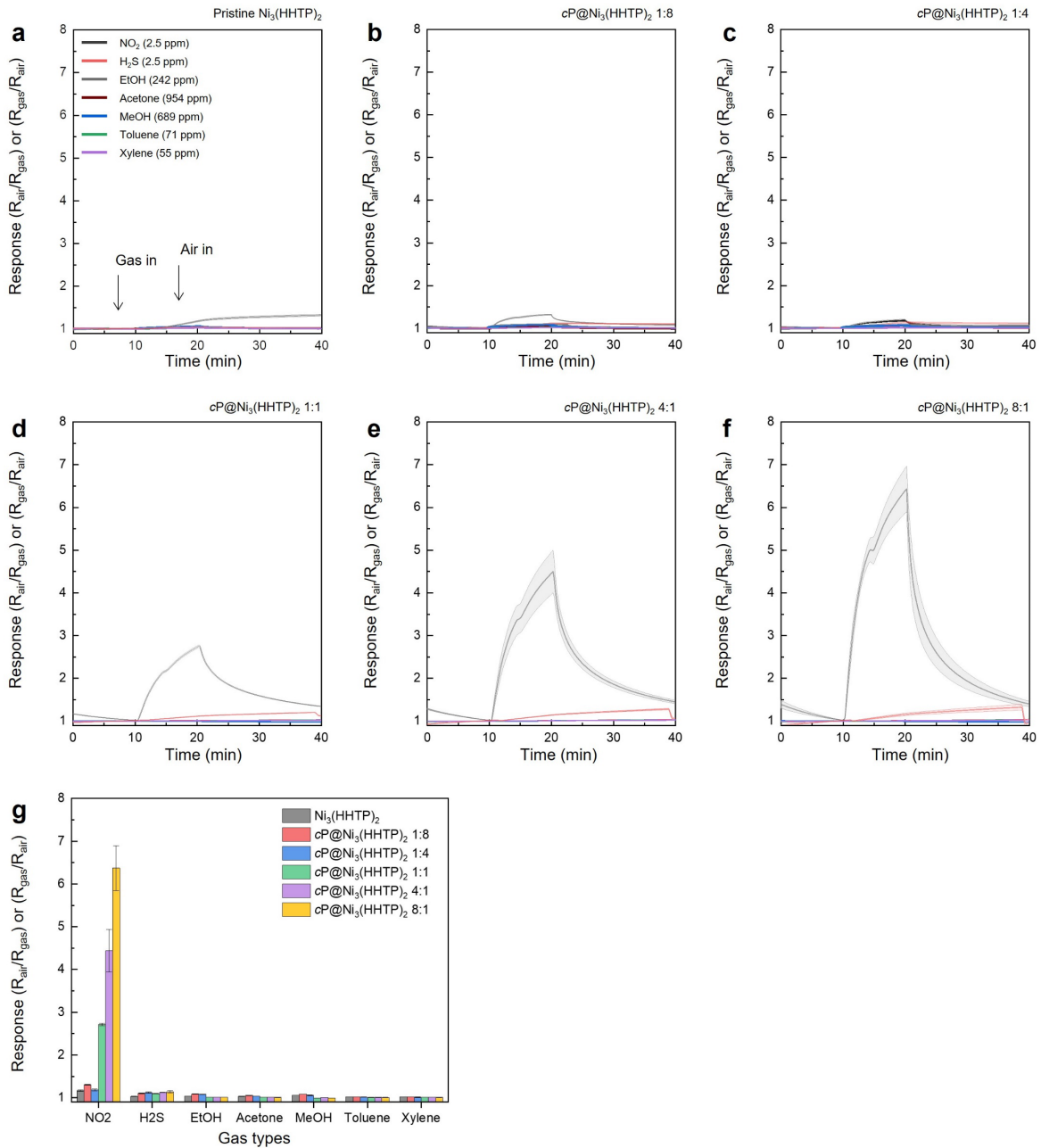
Supplementary Fig. 14 | Cyclic sensing tests of **a**, $\text{Ni}_3(\text{HHTP})_2$, **b**, $\text{Cu}_3(\text{HHTP})_2$, and **c**, $\text{Cu}_3(\text{HITP})_2$ -based sensors with various ratios between *cP* and *cMOFs*.



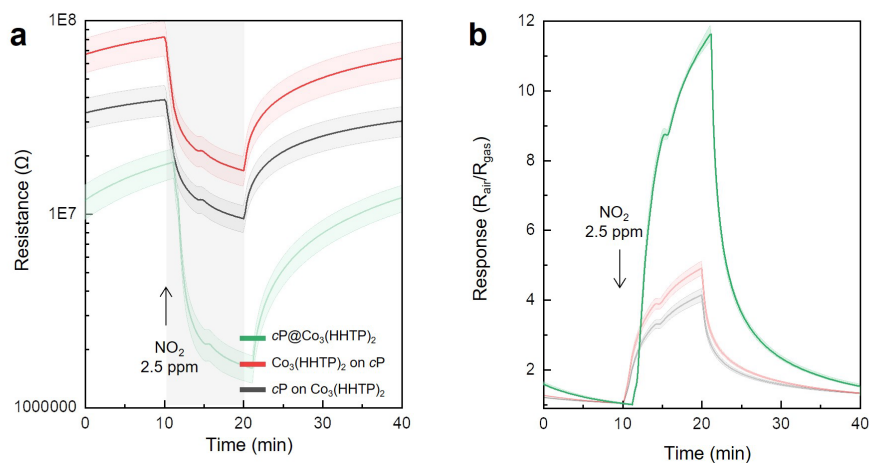
Supplementary Fig. 15 | Response and recovery fitting curves and raw response and recovery curves of **a**, $\text{cP@Co}_3(\text{HHTP})_2$ 1:1_1 μl , **b**, $\text{cP@Co}_3(\text{HHTP})_2$ 1:1_3 μl , and **c**, $\text{cP@Co}_3(\text{HHTP})_2$ 1:1_5 μl sensors. **d**, Corresponding adsorption and desorption rate constants of three different sensors. Sensors with reduced coating amounts (1 μl) exhibited faster reaction kinetics due to the extended gas diffusion time associated with thicker layers (coating of 3 μl or 5 μl).



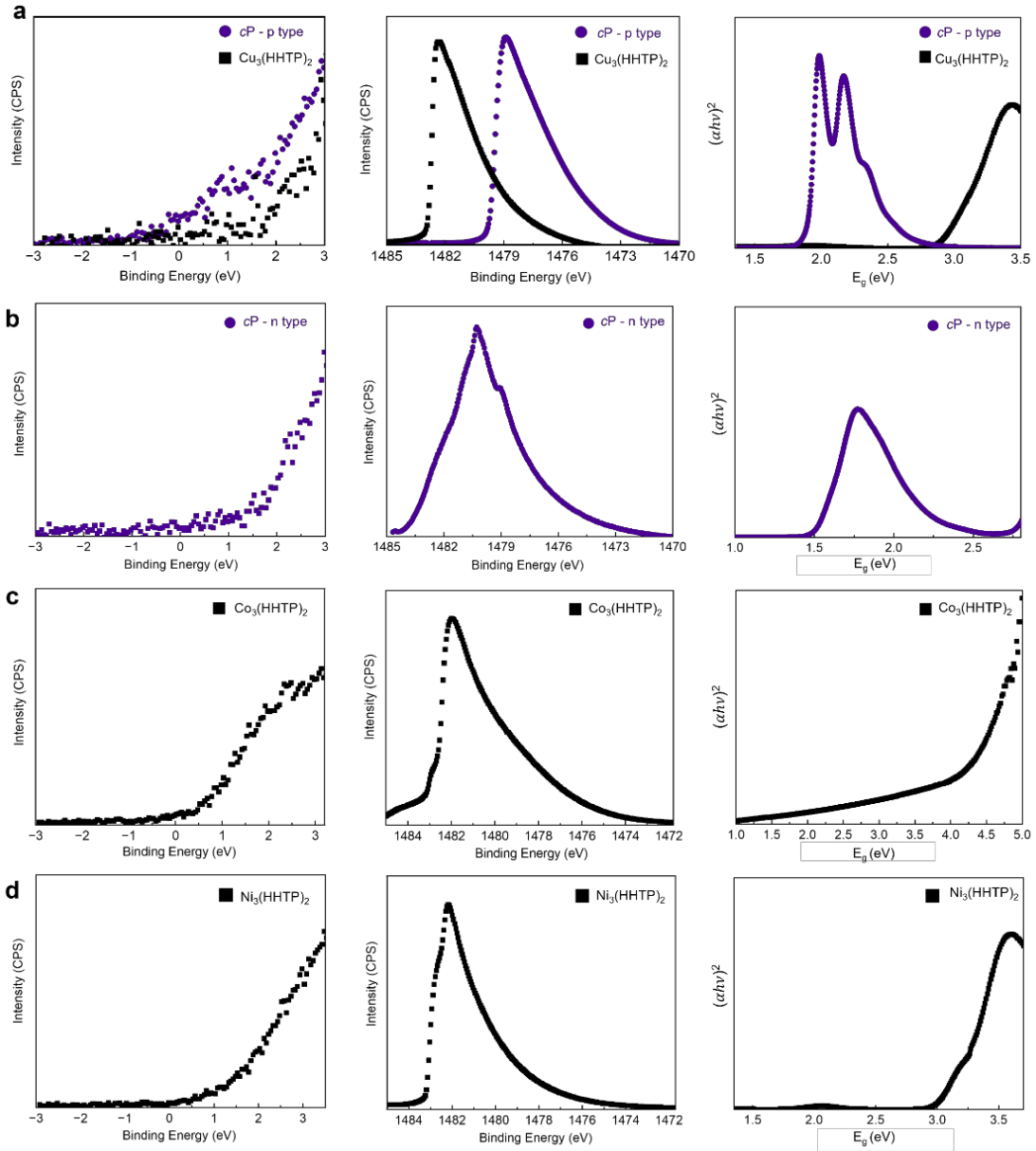
Supplementary Fig. 16 | Selectivity of **a**, $\text{Cu}_3(\text{HHTP})_2$, **b**, $\text{cP}@Cu_3(\text{HHTP})_2$ 1:8, **c**, $\text{cP}@Cu_3(\text{HHTP})_2$ 1:4, **d**, $\text{cP}@Cu_3(\text{HHTP})_2$ 1:1, **e**, $\text{cP}@Cu_3(\text{HHTP})_2$ 4:1, and **f**, $\text{cP}@Cu_3(\text{HHTP})_2$ 8:1. **g**, Overall response graphs ($N \geq 3$).

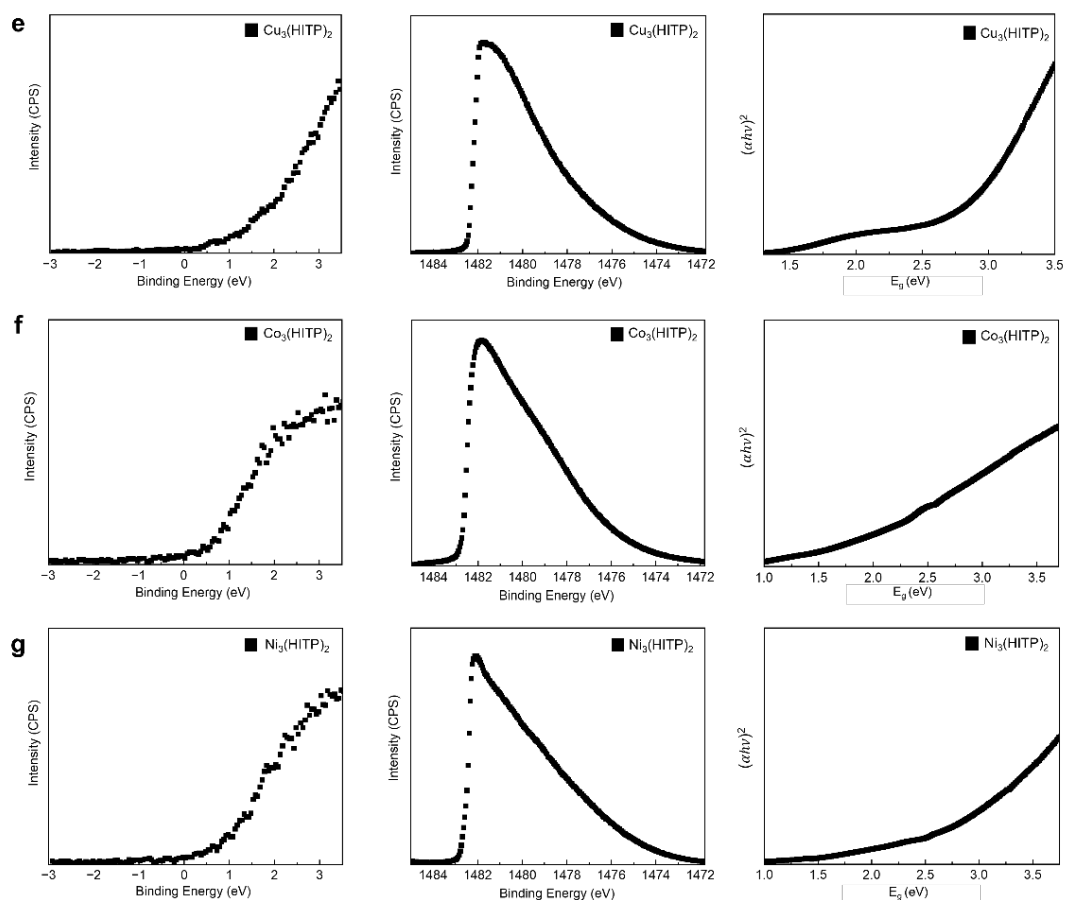


Supplementary Fig. 17 | Selectivity of **a**, $\text{Ni}_3(\text{HHTP})_2$, **b**, $\text{cP}@Ni_3(\text{HHTP})_2$ 1:8, **c**, $\text{cP}@Ni_3(\text{HHTP})_2$ 1:4, **d**, $\text{cP}@Ni_3(\text{HHTP})_2$ 1:1, **e**, $\text{cP}@Ni_3(\text{HHTP})_2$ 4:1, and **f**, $\text{cP}@Ni_3(\text{HHTP})_2$ 8:1. **g**, Overall response graphs ($N \geq 3$).



Supplementary Fig. 18 | **a**, Dynamic resistance transitions and **b**, response graphs of $cP@Co_3(HHTP)_2$ prepared by three different methods; i) finely mixed $cP@Co_3(HHTP)_2$, ii) $Co_3(HHTP)_2$ overlayer on cP , and iii) cP overlayer on $Co_3(HHTP)_2$ ($N = 3$).

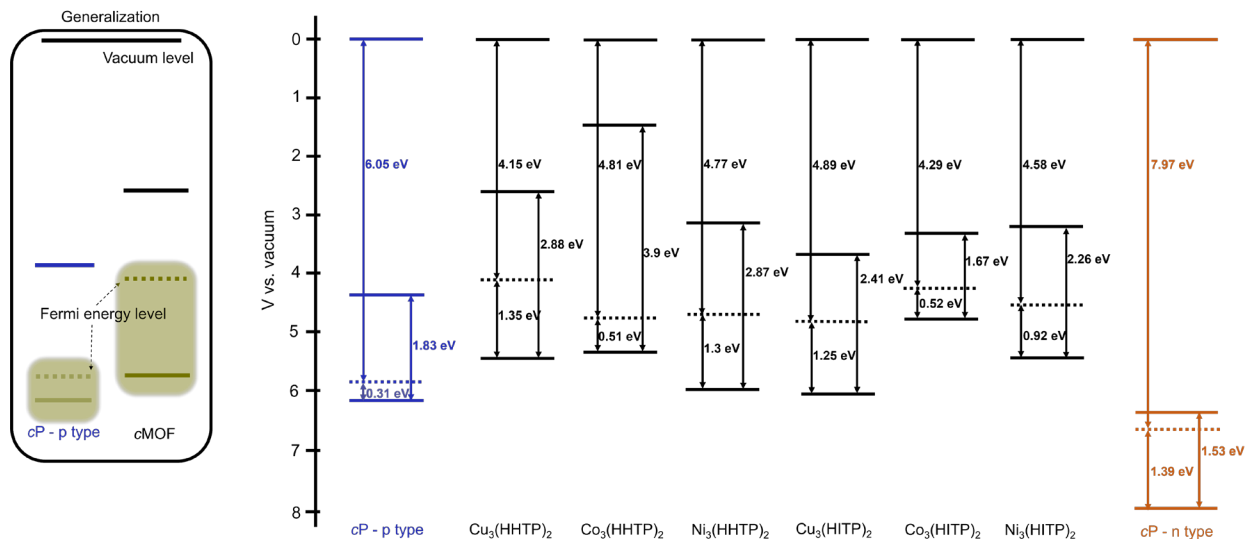




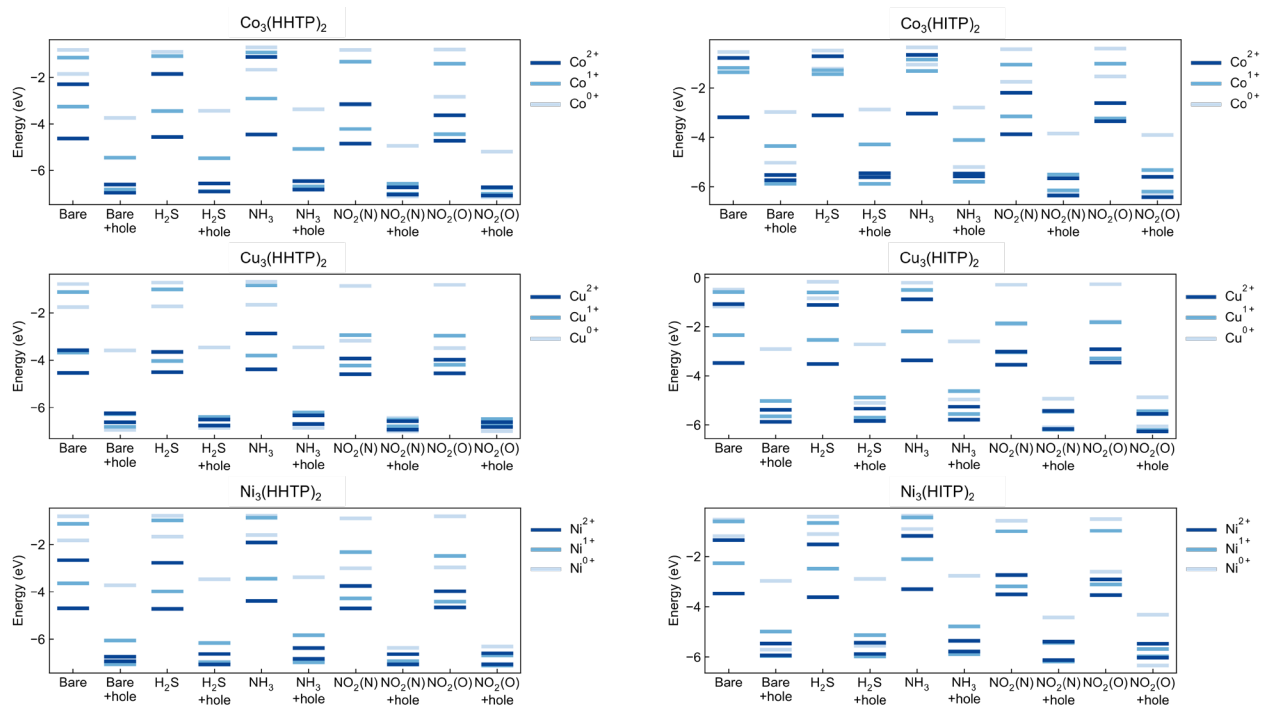
Supplementary Fig. 19 | XPS Cutoff curves (left), Fermi curves (middle), and Tauc plots (right), respectively, of *c*MOFs and *c*P. **a**, p-type *c*P and Cu₃(HHTP)₂. **b**, n-type *c*P. **c**, Co₃(HHTP)₂. **d**, Ni₃(HHTP)₂ **e**, Cu₃(HITP)₂. **f**, Co₃(HITP)₂. **g**, Ni₃(HITP)₂.

Supplementary Table. S1 | Summary of experimentally measured energy level details.

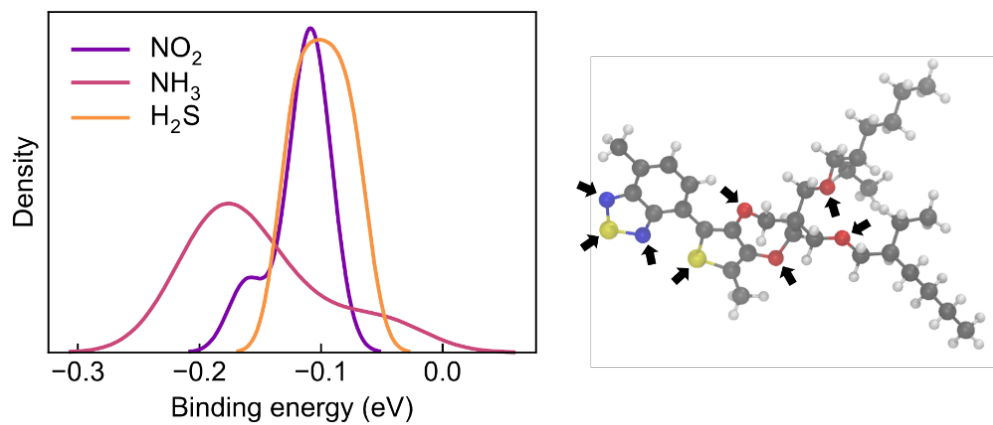
	p-type <i>c</i> P	n-type <i>c</i> P	Cu ₃ (HHTP) ₂	Ni ₃ (HHTP) ₂	Co ₃ (HHTP) ₂	Cu ₃ (HITP) ₂	Ni ₃ (HITP) ₂	Co ₃ (HITP) ₂
Photon E	1486.68 eV	1486.68 eV	1486.68 eV	1486.68 eV	1486.68 eV	1486.68 eV	1486.68 eV	1486.68 eV
Cutoff KE	11.25 eV	11.34 eV	13.77 eV	13.44 eV	13.89 eV	14.24 eV	14.05 eV	13.91 eV
Fermi KE	1492 eV	1490.05 eV	1496.29 eV	1495.34 eV	1495.76 eV	1496.02 eV	1496.15 eV	1496.3 eV
Work Function	6.05 eV	7.97 eV	4.15 eV	4.77 eV	4.81 eV	4.89 eV	4.580 eV	4.29 eV
E _F -E _V	0.31 eV	1.39 eV	1.25 eV	1.35 eV	0.51 eV	1.4 eV	0.92 eV	0.52 eV
E _g	1.83 eV	1.53 eV	2.88 eV	2.87 eV	3.9 eV	2.41 eV	3.9 eV	2.54 eV



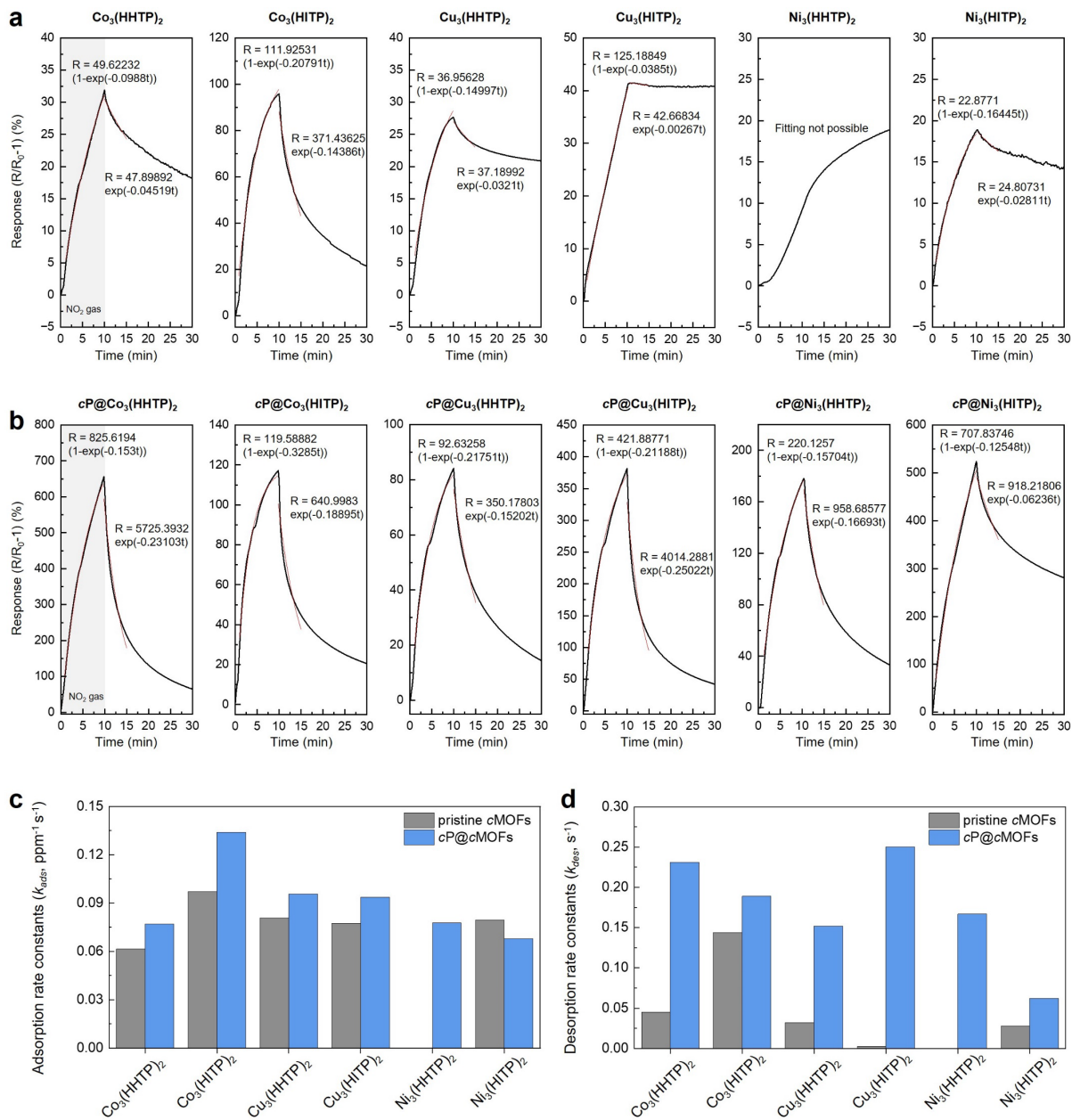
Supplementary Fig. 20 | Energy levels of cP and cMOFs used in the present work.



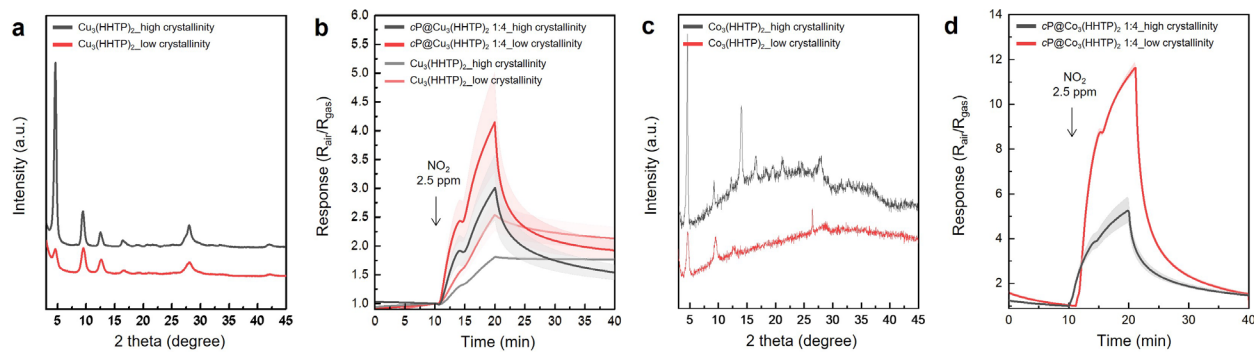
Supplementary Fig. 21 | HOMO and LUMO levels of cMOFs both with and without a hole, as well as with and without an adsorbate. All energy levels were calculated using the B3LYP functional and LACVP* basis set. $\text{NO}_2(\text{N})$ and $\text{NO}_2(\text{O})$ indicate N-binding and O-binding or NO_2 , respectively. The line color denotes the oxidation state of the metal.



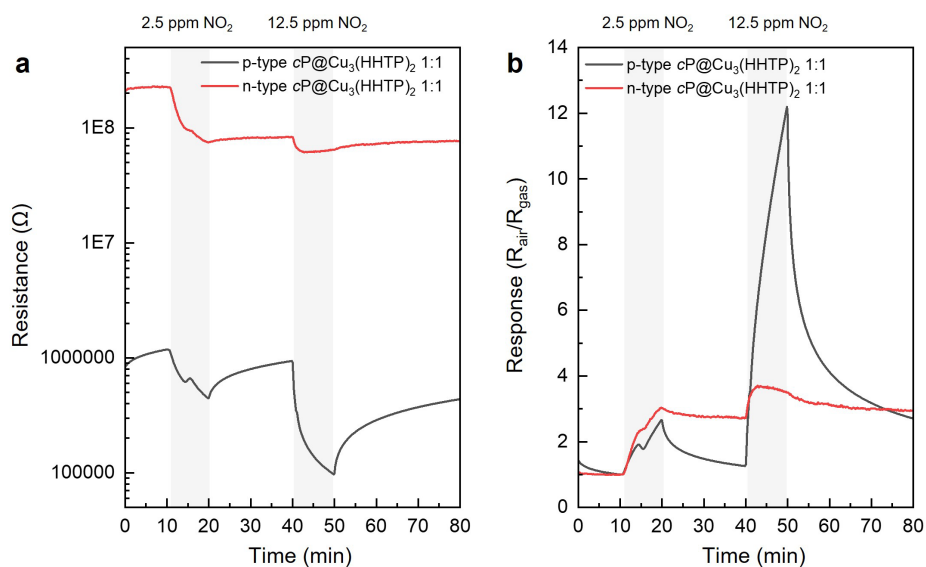
Supplementary Fig. 22 | Distribution of binding energies for NO₂, NH₃, and H₂S to different sites on the monomer of cP, as indicated by the arrow. N, O, and S atoms are considered as potential binding sites. The full monomer-adsorbate geometry was optimized using the B3LYP functional and LACVP* basis set. O: Red, N: Blue, H: White, S: Yellow.



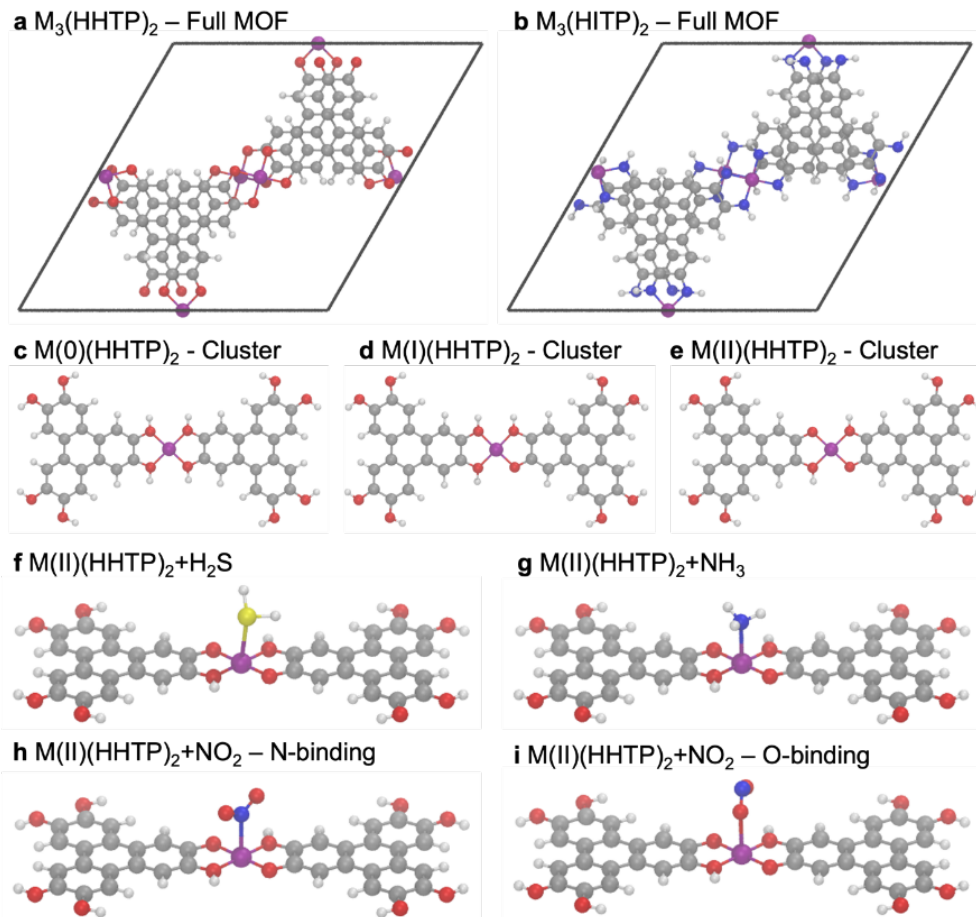
Supplementary Fig. 23 | Response and recovery fitting curves of **a**, six different cMOFs and **b**, cP@cMOFs 1:1 composite. The corresponding **c**, adsorption and **d**, desorption rate constants.



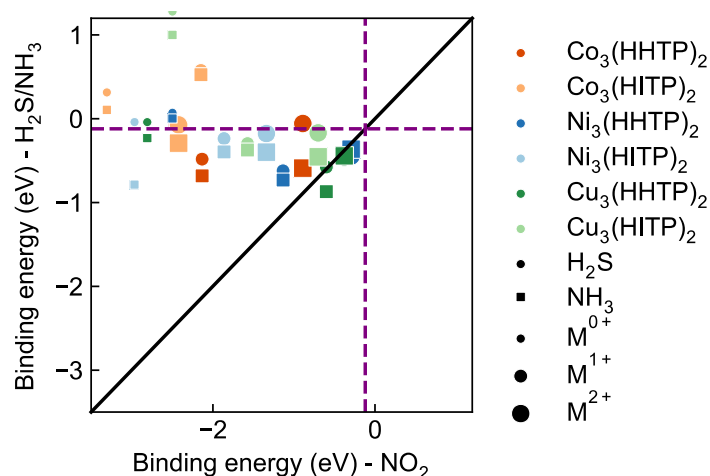
Supplementary Fig. 24 | **a**, XRD analysis of $\text{Cu}_3(\text{HHTP})_2$ with high and low crystallinity. **b**, NO_2 sensing response of $\text{cP}@Cu_3(\text{HHTP})_2$ and pristine $\text{Cu}_3(\text{HHTP})_2$ using high and low crystallinity of cMOFs ($N \geq 3$). **c**, XRD analysis of $\text{Co}_3(\text{HHTP})_2$ with high and low crystallinity. **d**, NO_2 sensing response of $\text{cP}@Co_3(\text{HHTP})_2$ with high and low crystallinity ($N \geq 3$).



Supplementary Fig. 25 | **a**, Dynamic resistance transitions and **b**, response graphs of p-type $\text{cP}@Cu_3(\text{HHTP})_2$ 1:1 and n-type $\text{cP}@Cu_3(\text{HHTP})_2$ 1:1 upon sequential exposure to 2.5 ppm and 12.5 ppm NO_2 gas.



Supplementary Fig. 26 | Top view of the complete *c*MOF structures for **a**, $M_3(\text{HHTP})_2$ and **b**, $M_3(\text{HITP})_2$. The black outline indicates the boundaries of the unit cell. Clusters of $M_3(\text{HHTP})_2$ are shown for various oxidation state of the metal: **c**, +0, **d**, +1, and **e**, +2. Note the differing numbers of hydrogen atoms on the metal-coordinating oxygens used to alter the metal oxidation state. Clusters of $M_3(\text{HHTP})_2$ are also illustrated while binding with molecules: **f**, H_2S , **g**, NH_3 , **h**, NO_2 with nitrogen atom binding, and **i**, NO_2 with oxygen atom binding. M: Purple, C: Grey, O: Red, N: Blue, H: White.



Supplementary Fig. 27 | Binding energy of H₂S and NH₃ to the MOF compared with that of NO₂. The purple dashed line represents the average binding energy between the cP monomer and the gas molecules. A black line indicates parity.

4) Supplementary References

1. Giovannitti, A., *et al.* Redox-Stability of Alkoxy-BDT Copolymers and their Use for Organic Bioelectronic Devices. *Adv. Funct. Mater.* **28**, 1706325 (2018).
2. Giovannitti, A., *et al.* The role of the side chain on the performance of n-type conjugated polymers in aqueous electrolytes. *Chem. Mater.* **30**, 2945-2953 (2018).
3. Nam, K. W., *et al.* Conductive 2D metal-organic framework for high-performance cathodes in aqueous rechargeable zinc batteries. *Nat. Commun.* **10**, (2019).
4. Foster, M. E., Sohlberg, K., Spataru, C. D. & Allendorf, M. D. Proposed Modification of the Graphene Analogue Ni₃(HITP)₂ to Yield a Semiconducting Material. *J. Phys. Chem. C.* **120**, (2016).
5. Kresse, G., & Hafner, J. Ab initio molecular dynamics for liquid metals. *Phys. Rev. B.* **47**, 558 (2014).
6. Kresse, G., & Furthmüller, J. Efficiency of ab-initio total energy calculations for metals and semiconductors using a plane-wave basis set. *Comput. Mater. Sci.* **6**, 15-50 (1996).
7. Kresse, G., & Furthmüller, J. Efficient iterative schemes for ab initio total-energy calculations using a plane-wave basis set. *Phys. Rev. B.* **54**, 11169 (1996).
8. Kresse, G., & Joubert, D., From ultrasoft pseudopotentials to the projector augmented-wave method. *Phys. Rev. B.* **59**, 1758 (1999).
9. Perdew, J. P., Burke, K., & Ernzerhof, M. Generalized gradient approximation made simple. *Phys. Rev. Lett.* **77**, 3865 (1996).
10. Blöchl, P. E. Projector augmented-wave method. *Physical review B* **50**, 17953 (1994).
11. Grimme, S. Semiempirical GGA-type density functional constructed with a long-range dispersion correction. *J. Comput. Chem.* **27**, 1787-1799 (2006).
12. Ufimtsev, I. S., & Martinez, T. J. Graphical processing units for quantum chemistry. *Comput. Sci. Engin.* **10**, 26-34 (2008).
13. Becke, A. D. A new mixing of Hartree-Fock and local density-functional theories. *J. Chem. Phys.* **98**, 1372-1377 (2008).

14. Lee, C., Yang, W., & Parr, R. G. Development of the Colle-Salvetti correlation-energy formula into a functional of the electron density. *Phys. Rev. B.* **37**, 785 (1988).
15. Vosko, S. H., Wilk, L., & Nusair, M. Accurate spin-dependent electron liquid correlation energies for local spin density calculations: a critical analysis. *Canad. J. Phys.* **58**, 1200-1211 (1980).
16. Hay, P. J., & Wadt, W. R. Ab initio effective core potentials for molecular calculations. Potentials for the transition metal atoms Sc to Hg. *J. Chem. Phys.* **82**, 270-283 (1985).
17. Wang, L.-P., & Song, C., Geometry optimization made simple with translation and rotation coordinates. *J. Chem. Phys.* **144**, (2016).
18. Chen, L., *et al.* Noncovalently netted, photoconductive sheets with extremely high carrier mobility and conduction anisotropy from triphenylene-fused metal trigon conjugates. *J. Am. Chem. Soc.* **131**, 7287-7292 (2009).